JGR Oceans

Key Points:

- Interannual variations in the thickness and volume of modified Circumpolar Deep Water intensify southward toward Dotson Ice Shelf
- Modified Circumpolar Deep Water volume in the Dotson-Getz Trough was 8,000 km³ in 2007, 4,700 km³ in 2014, and 7,300 km³ in 2018
- Dominant south-southeast wind over the Dotson-Getz Trough intensified Ekman upwelling at the eastern boundary of the Amundsen Sea polynya

Author Contributions:

Conceptualization: Tae-Wan Kim
Data curation: Hee Won Yang
Formal analysis: Tae-Wan Kim
Funding acquisition: Jisoo Park, SangHoon Lee
Investigation: Tae-Wan Kim, Hee Won Yang, Yeong Gi Kim, Ho Kyung Ha, Chang-Sin Kim, Kyoung-Ho Cho, Taewook Park, SangHoon Lee
Methodology: Tae-Wan Kim
Project Administration: Jisoo Park, SangHoon Lee
Resources: Anna K. Wåhlin
Validation: Tae-Wan Kim
Visualization: Tae-Wan Kim

Interannual Variation of Modified Circumpolar Deep Water in the Dotson-Getz Trough, West Antarctica

Tae-Wan Kim[1] [ID], **Hee Won Yang**[1,2], **Pierre Dutrieux**[3] [ID], **Anna K. Wåhlin**[4], **Adrian Jenkins**[5] [ID], **Yeong Gi Kim**[1,2], **Ho Kyung Ha**[6] [ID], **Chang-Sin Kim**[7] [ID], **Kyoung-Ho Cho**[1] [ID], **Taewook Park**[1], **Jisoo Park**[1] [ID], **SangHoon Lee**[1] [ID], and **Yang-Ki Cho**[2] [ID]

[1]Korea Polar Research Institute, Incheon, South Korea, [2]School of Earth and Environmental Sciences/Research Institute of Oceanography, Seoul National University, Seoul, South Korea, [3]British Antarctic Survey, Natural Environment Research Council, Cambridge, UK, [4]Department of Marine Sciences, University of Gothenburg, Gothenburg, Sweden, [5]Department of Geography and Environmental Sciences, Northumbria University, Newcastle upon Tyne, UK, [6]Department of Ocean Sciences, Inha University, Incheon, South Korea, [7]National Institute of Fisheries Science, Busan, South Korea

Abstract Widespread ice shelf thinning has been recorded in the Amundsen Sea in recent decades, driven by basal melting and intrusions of relatively warm Circumpolar Deep Water (CDW) onto the continental shelf. The Dotson Ice Shelf (DIS) is located to the south of the Amundsen Sea polynya, and has a high basal melting rate because modified CDW (mCDW) fills the Dotson-Getz Trough (DGT) and reaches the base of the ice shelf. Here, hydrographic data in the DGT obtained during seven oceanographic surveys from 2007 to 2018 were used to study the interannual variation in mCDW volume and properties and their causes. Although mCDW volume showed relatively weak interannual variations at the continental shelf break, these variations intensified southward and reached a maximum in front of the DIS. There, the mCDW volume was ~8,000 km³ in 2007, rapidly decreased to 4,700 km³ in 2014 before rebounding to 7,300 km³ in 2018. We find that such interannual variability is coherent with local Ekman pumping integrated along the DGT modulated by the presence of sea ice, and complementing earlier theories involving shelf break winds only. The interannual variability in strength of the dominant south-southeast coastal wind modulates the amplitude of Ekman upwelling along the eastern boundary of the Amundsen Sea polynya during the austral summers of the surveyed years, apparently leading to change in the volume of mCDW along the DGT. We note a strong correlation between the wind variability and the longitudinal location of the Amundsen Sea Low.

Plain Language Summary Recent widespread thinning of floating ice shelves around the Amundsen Sea coast has been shown to result from flows of relatively warm water into ocean cavities below the ice shelves. Dotson Ice Shelf is located in the center of the Amundsen Sea, and has seen high rates of ice loss from ocean-driven melting as warm water spreads southward from the Southern Ocean along the Dotson-Getz Trough. We analyzed long-term hydrographic observations from seven oceanographic surveys along the trough between 2007 and 2018 to understand the variation of warm water properties. We show that the warm water volume varies significantly from year to year, and that this variability is largely driven by local winds which are, in turn, connected to the broader scale atmospheric circulation. These results provide insights into how variability in atmospheric circulation due to climate change will affect the water masses on the Antarctic coast and how rapidly ice shelves will melt.

1. Introduction

In recent decades, Antarctic ice sheets have rapidly retreated, thus contributing to rising sea levels. An estimated 2720 billion tonnes of ice was lost from Antarctica between 1992 and 2017, corresponding to a global sea-level rise of about 7.6 mm (Shepherd et al., 2018). In particular, grounded ice reduction in West Antarctica accounted for ~86% of the total Antarctic ice loss. The rapid ice reduction in West Antarctica caused by the increase in glacial flow is believed to be driven by the thinning of the buttressing ice shelves, in turn associated with increasing ocean melt. Notably, the fastest rate of decline in ice volume was observed in the Amundsen Sea sector during the late 2000s (Turner et al., 2017), with some potential anthropogenic origins (Holland et al., 2019).

The Dotson Ice Shelf (DIS) is about 70 km long and 50 km wide, and is situated between the Martin Peninsula (MP) and the Bear Peninsula (BP) on the Marie Byrd Land coast, in the Amundsen Sea embayment, West Antarctica (Figure 1). It buttresses the flow of the Kohler and Smith glaciers. A rapid thinning of the DIS has been

Writing – original draft: Tae-Wan Kim, Adrian Jenkins
Writing – review & editing: Tae-Wan Kim, Pierre Dutrieux, Anna K. Wåhlin, Yeong Gi Kim, Ho Kyung Ha, Chang-Sin Kim, Taewook Park, Yang-Ki Cho

revealed from satellite radar altimeter observations (e.g., Adusumilli et al., 2020; Gourmelen et al., 2017; Paolo et al., 2015). Between 1994 and 2012, the thinning rate of the DIS was >30% faster than the mean rate of the Amundsen Sea sector (Paolo et al., 2015). In addition, a 35 km grounding line retreat has been measured at the Kohler and Smith glaciers between 1992 and 2011, which is the fastest observed retreat within the Amundsen Sea sector (Rignot et al., 2014).

Thinning of the DIS is mainly due to basal melting (Depoorter et al., 2013), which is affected by the intrusion of relatively warm and salty modified Circumpolar Deep Water (mCDW) to the ice shelf cavities (Jenkins et al., 2018). CDW sourced in the nearby Southern Ocean is transported onto the continental shelf and cools and freshens by interacting with Antarctic surface water (AASW), resulting in mCDW (Wåhlin et al., 2010). This mCDW flows along the Dotson-Getz Trough (DGT), reaches the bottom of the DIS, and transfers oceanic heat to the ice shelf (Ha et al., 2014). Jenkins et al. (2018) showed that the large decadal variability of oceanic heat content in front of the DIS cavity, mostly associated with mCDW properties and volume, affects heat transport into the cavity, ice shelf melt, and grounding line movements. Therefore, understanding the transport in and the thickness of the mCDW layer in the DGT and their variability is key for investigating the thinning process of the DIS.

Many scholars have investigated the variability and mechanism of mCDW flowing into the DGT based on field observations (e.g., Dotto et al., 2020; Kim et al., 2017; Wåhlin et al., 2012, 2013). Wåhlin et al. (2012) argued that the intrusion of warm and salty water over the continental slope may be due to upslope transport in the bottom Ekman layer. A 2-year-long mooring dataset for the DGT further showed that the mean near-bottom southward current velocity is correlated with the westerly wind at the shelf break (Carvajal et al., 2013; Wåhlin et al., 2013). Using the same mooring observations, Kim et al. (2017) demonstrated that the seasonal variability of the warm layer was influenced by Ekman upwelling. More recently, Dotto et al. (2020) analyzed multi-year mooring data from the DGT to determine the variability and cause of CDW inflowing onto the continental shelf. The authors concluded that the weakening of this inflow was a response to the strengthening of easterly winds at the shelf break, which is associated with the Amundsen Sea Low (ASL), a climatological low-pressure system located in the southern Pacific Ocean (e.g., Turner et al., 2017). These results are all consistent with similar work done in the Eastern Amundsen Sea, where easterly winds variability at the shelf break also appear to modulate oceanic heat content (Dutrieux et al., 2014).

Many modeling studies have been conducted to investigate the delivery of mCDW to the continental shelf and its mechanism in the Amundsen Sea Embayment (e.g., Dotto et al., 2019; Kimura et al., 2017; Thoma et al., 2008). Thoma et al. (2008) first showed that changing the regional wind field affected the variability of the warm mCDW inflow onto the continental shelf around Pine Island Bay. According to their numerical model, the strengthening of the westerly winds over the shelf break was associated with upwelling and an increased intrusion of CDW along the shelf break. Kimura et al. (2017) used a regional model to identify the effects of the wind field and sea ice motion on the onshore advection of warm water in the deep Pine Island-Thwaites Trough and the DGT. The onshore heat transport along these troughs was correlated with the total surface stress and its curl, although the seasonal cycle of the CDW layer thickness exhibited differences between the calving fronts of the Pine Island Glacier (PIG) and DIS. Dotto et al. (2019) further analyzed the results of Kimura et al. (2017), and argued that changes in the oceanic heat content in the DGT were controlled by changing water mass properties along the same isopycnal, while the Pine Island-Thwaites Trough saw larger contributions from isopycnal vertical displacements.

The volume of CDW flowing into the DGT beyond the shelf break therefore appears to be influenced by the variability of the wind field and atmospheric circulation at the shelf break. In turn, the atmospheric circulation over the Amundsen Sea is much more varied than any other sea in the Antarctic Ocean (Connolley, 1997) due to the variability of the depth and location of the ASL (Hosking et al., 2013). The longitudinal location of the ASL shows distinct seasonal migration and interannual variability, influenced both by the phase of the Southern Annular Mode (SAM) and the El Niño–Southern Oscillation (ENSO) (Fogt et al., 2011). But many local processes can influence mCDW volume and properties as it travels southward from the shelf break. Assuming that the average southward velocity of mCDW in DGT is 2.4 cm s^{-1} (Wåhlin et al., 2013), a 300 km pathway along the DGT would take 4–5 months, allowing for extensive modulation and aliasing by seasonal processes (Kim et al., 2017; Webber et al., 2017). In particular, atmospheric forcing along the boundary of the polynya in DGT, which develops widely in the austral summer, also varies from year to year, and thus may affect the interannual variability of the volume of mCDW in the DGT. Therefore, to understand the interannual variability of the mCDW volume in front of the DIS, which is directly related to ice shelf melting, it is necessary to understand
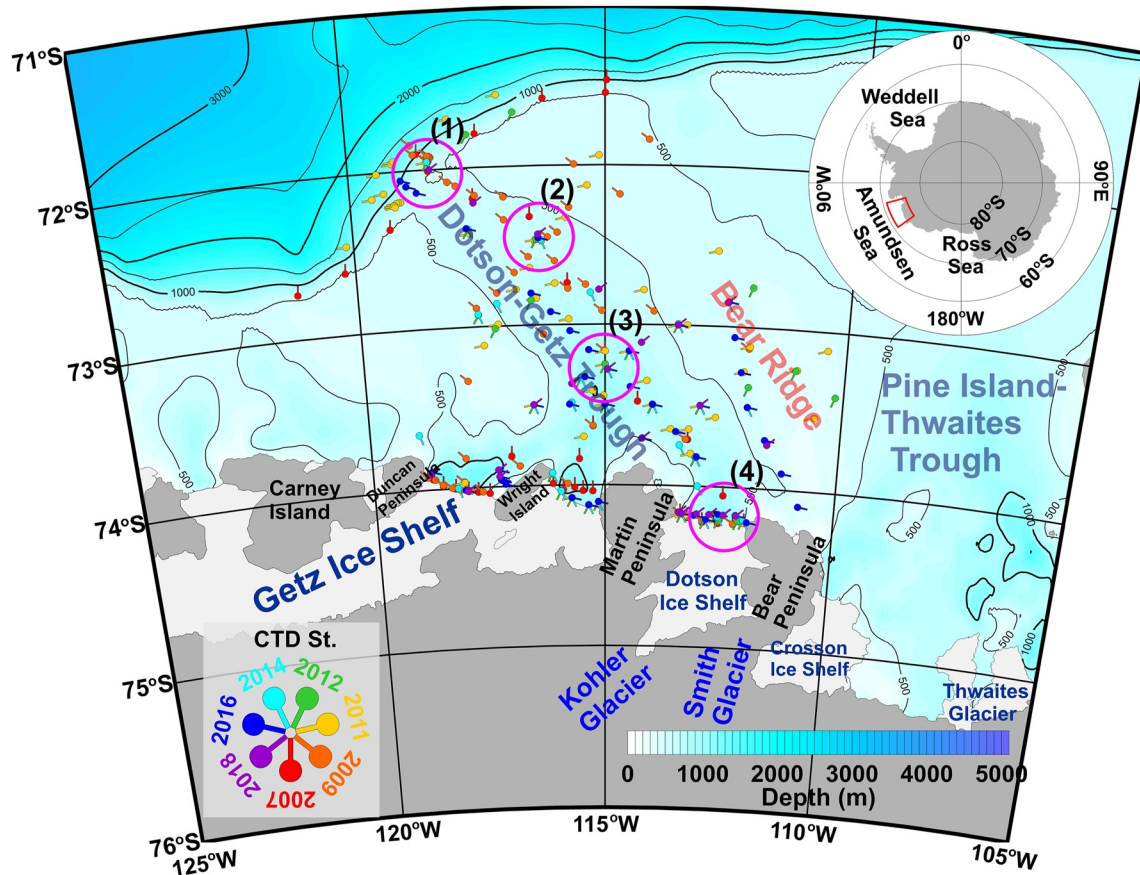
Figure 1. Map of study area showing the conductivity–temperature–depth (CTD) stations and seabed depth obtained from the Multibeam-swath bathymetry (Nitsche et al., 2007). Floating glacial ice (ice shelves) is shown in mid-gray. Color-coded symbols represent CTD observation stations for each year. Magenta circles represent the four main areas of the DGT, which will be described in Section 3.1: (1) the entrance of DGT, (2) the northern side of DGT, (3) the center of the Amundsen Sea polynya, and (4) the Dotson Ice Shelf front.

the spatio-temporal variability of mCDW in the DGT and the local (in the trough) and remote (at the shelf break) forcing of this variability. This study identifies the spatial and interannual variabilities of the mCDW volume along the DGT based on seven summer hydrographic campaign observations during 2007–2018 and investigates the causes of variability in mCDW. We find that local forcing does have a role to play. After reviewing data and methods (Section 2), we analyze the spatial gradients in the mCDW distribution and its temporal evolution and detail how local variability in sea ice distribution and winds coherently conspire to explain the observed variability (Section 3). The relationship between this variability and that at the shelf break or larger scale atmospheric forcing is discussed in Section 4.

2. Data and Methods

2.1. Hydrographic Data Collection

This study uses hydrographic data from seven expeditions undertaken in austral summer on three ice breaker research vessels (R/Vs *Nathaniel B. Palmer*, *Oden*, and *Araon*) in and around the DGT (Figure 1). At all stations, profiles of temperature, salinity, and dissolved oxygen (DO) were sampled with a Sea-Bird Scientific SBE 911+ conductivity–temperature–depth (CTD) profiling system. All data (Table 1) were subsequently calibrated and quality controlled before being averaged into 1 m depth intervals.

Table 1
Research Cruise Information for the Conductivity–Temperature–Depth (CTD) and Dissolved Oxygen (DO) Data Used in This Study

Year (for analysis)	Cruise name	Research vessel	Survey dates	Number of stations	Instruments
2007	NBP0702	*Nathaniel B Palmer*	February 19 to March 12, 2007	36	CTD, DO
2009	NBP0901	*Nathaniel B Palmer*	February 2–15, 2009	29	CTD, DO
	Oden 2008/09	*Oden*	December 17–23, 2008	23	CTD, DO
2011	NBP1005	*Nathaniel B Palmer*	December 14, 2010 to January 6, 2011	21	CTD, DO
	Oden 2010/11	*Oden*	December 21–28, 2010	18	CTD, DO
	ANA01C	*Araon*	December 29, 2010 to January 8, 2011	21	CTD, DO
2012	ANA02C	*Araon*	February, 10 to March 4, 2012	31	CTD, DO
2014	ANA04B	*Araon*	January 1–14, 2014	32	CTD, DO
2016	ANA06B	*Araon*	January 15 to February 6, 2016	45	CTD, DO
2018	ANA08B	*Araon*	January 21–30, 2018	23	CTD, DO

2.2. Calculation of mCDW Ratio

As identified in previous studies, the temperature, salinity, and DO of mCDW in the DGT are partly determined by mixing with AASW over the continental shelf. These variables exhibit an interannual variability because the volume and properties of CDW intrusion to the DGT and their interactions with local water masses are not constant. In this study, the mCDW volume at each station in each year was calculated to identify the interannual spatial variability of mCDW in the DGT and the local causes of its change. To do so, we first estimate the mixing ratio of mCDW, winter water (WW), and ice and the temperature, salinity, and DO end members were defined for each water mass in each year (Figure 2, Table 2). The temperature, salinity, and DO of ice were assumed to be constant in all years at $-95°C$ (includes the effect of the heat necessary to melt the glacial ice), 0 PSU, and 24.5 mL kg^{-1} (Jenkins et al., 2018).

Assuming that the ice–seawater system is closed, the seawater in the DGT can be defined as a mixture of mCDW, WW, and ice meltwater (Jenkins, 1999; Jenkins & Jacobs, 2008). This excludes the sea surface layer, which is highly influenced by exchange with the atmosphere. Therefore, most observed data fell within a triangle formed by the connection of the mCDW, WW, and ice end members in the 2D diagram between properties (temperature, salinity, and DO). The potential temperature (θ) and salinity (S) end members of mCDW and WW were defined from Figures 2a and 2b. Jenkins et al. (2018) defined the end member of mCDW at the intersection of observed deep water properties and the meltwater mixing line. This definition allows for a more accurate estimation of the ice meltwater fraction originating from the DIS because it omits the warmest water near the bottom, which does not contribute to ice shelf melting. However, in this study, to estimate the mCDW volume ratio in the DGT, we defined the temperature and salinity end members of mCDW at the point of highest density in all observed data.

WW is formed when seawater freezes at the sea surface due to heat exchange with the atmosphere during winter. During sea ice growth, WW, whose temperature is near the surface freezing point, occupies a very thick layer, from the surface to the mCDW layer, as a result of vertical convection. However, pure WW formed in winter is diluted through mixing with sea ice and glacial meltwater during the summer. The end member of pure WW was defined in this study as the intersection of the extension line of the mCDW end member containing the observed point and the seawater surface freezing line (Figure 2b). The DO end members were defined as the intersection between the mCDW/WW mixing line and the previously defined θ end members of mCDW and WW (Figure 2c).

The observed in situ seawater properties of θ, S, and DO can be expressed by the calculation formulae of end members, the ice meltwater fraction (V_{ice}), the volume ratio of mCDW (V_{mCDW}) and WW (V_{WW}). Therefore, three simultaneous equations can be written; two related to the properties of seawater, and the third stating that the sum of each partial volume equals 1:

$$\chi_{Obs}^1 = \chi_{Ice}^1 V_{Ice} + \chi_{WW}^1 V_{WW} + \chi_{mCDW}^1 V_{mCDW} \tag{1}$$

$$\chi_{Obs}^2 = \chi_{Ice}^2 V_{Ice} + \chi_{WW}^2 V_{WW} + \chi_{mCDW}^2 V_{mCDW} \tag{2}$$
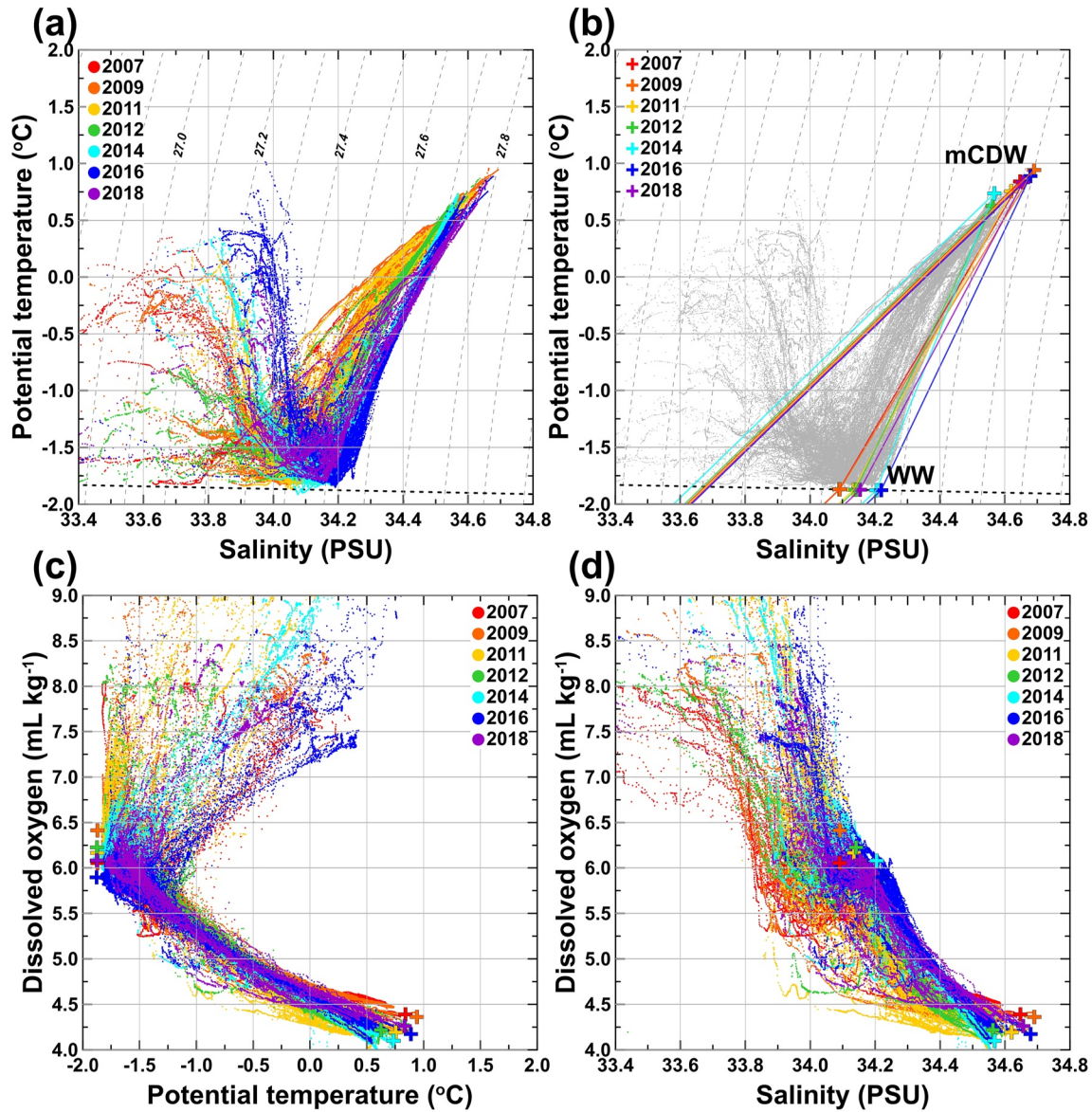
Figure 2. Scatter plots of potential temperature (θ), Salinity (S), and dissolved oxygen (DO) in the Dotson-Getz Trough for seven nonconsecutive years (a–d). (a) The color-coded dots represent the observed data in the θ–S space. The gray dash lines are contours of sigma-t in 0.1 kg m^{-3} increments, and the black dash line indicates the surface seawater freezing point. (b) Color-coded cross (+) symbols represent the estimated end member of modified Circumpolar Deep Water (mCDW) and winter water (WW) and connecting lines between the end members of two water masses and ice for individual years. (c) Same as (a) in the DO–θ space. (d) Same as (a) in the DO–S space.

$$V_{\text{Ice}} + V_{\text{WW}} + V_{\text{mCDW}} = 1 \tag{3}$$

In Equations 1–3, χ^1 and χ^2 represent either θ, S, or DO, and the subscripts Ice, mCDW, WW, and Obs indicate the end members of ice, mCDW, WW, and in situ observations, respectively. From Equations 1–3, V_{ice}, V_{mCDW}, and V_{WW} can be calculated as follows:

Table 2
End Members of Temperature (T), Salinity (S), and Dissolved Oxygen (DO) in Modified Circumpolar Deep Water (mCDW), Winter Water (WW), and Ice in the Dotson-Getz Trough for Seven Nonconsecutive Years During 2007–2018

	mCDW properties			WW properties			Ice properties		
Year	T (°C)	S (PSU)	DO (mL kg^{-1})	T (°C)	S (PSU)	DO (mL kg^{-1})	T (°C)	S (PSU)	DO (mL kg^{-1})
2007	0.840	34.648	4.391	−1.870	34.091	6.052	−95	0	24.5
2009	0.941	34.690	4.362	−1.870	34.092	6.415			
2011	0.754	34.620	4.192	−1.873	34.135	6.164			
2012	0.625	34.562	4.218	−1.873	34.141	6.225			
2014	0.735	34.568	4.100	−1.877	34.204	6.078			
2016	0.888	34.679	4.174	−1.878	34.219	5.894			
2018	0.832	34.656	4.262	−1.874	34.154	6.081			

$$V_{\text{Ice}} = \frac{\left(\chi_{\text{Obs}}^2 - \chi_{\text{mCDW}}^2\right) - \left(\chi_{\text{Obs}}^1 - \chi_{\text{mCDW}}^1\right)\dfrac{\left(\chi_{\text{WW}}^2 - \chi_{\text{mCDW}}^2\right)}{\left(\chi_{\text{WW}}^1 - \chi_{\text{mCDW}}^1\right)}}{\left(\chi_{\text{Ice}}^2 - \chi_{\text{mCDW}}^2\right) - \left(\chi_{\text{Ice}}^1 - \chi_{\text{mCDW}}^1\right)\dfrac{\left(\chi_{\text{WW}}^2 - \chi_{\text{mCDW}}^2\right)}{\left(\chi_{\text{WW}}^1 - \chi_{\text{mCDW}}^1\right)}} \tag{4}$$

$$V_{\text{WW}} = \frac{\left(\chi_{\text{Obs}}^1 - \chi_{\text{mCDW}}^1\right) - \left(\chi_{\text{Ice}}^1 - \chi_{\text{mCDW}}^1\right)V_{\text{Ice}}}{\left(\chi_{\text{WW}}^1 - \chi_{\text{mCDW}}^1\right)} \tag{5}$$

$$V_{\text{mCDW}} = \frac{\left(\chi_{\text{Obs}}^1 - \chi_{\text{WW}}^1\right) - \left(\chi_{\text{Ice}}^1 - \chi_{\text{WW}}^1\right)V_{\text{Ice}}}{\left(\chi_{\text{mCDW}}^1 - \chi_{\text{WW}}^1\right)} \tag{6}$$

V_{mCDW} and V_{WW} calculated from only two seawater properties (θ–S, DO–S, or DO–θ) showed, respectively, a significant difference over the upper 100 m due to solar heating and sea ice melting during austral summer (Biddle et al., 2017). Air-sea interaction at the sea surface can also affect dissolved oxygen concentrations over the upper 100 m. As a result, the ratio of mCDW calculated from θ-S tends to be overestimated in the upper layer due to solar heating, while that of WW is underestimated. In contrast, the ratio of mCDW calculated from DO-θ and DO-S is underestimated due to the addition of oxygen through air-sea interaction in the surface layer, and that of WW is overestimated. In the following, we compute profiles of V_{ice}, V_{mCDW}, and V_{WW} at each station averaging their estimates in the three-property space (θ–S, DO–S, and DO–θ) and we disregard the upper 200 m, where uncertainties are higher. We then integrate V_{mCDW} in depth to estimate a mCDW volume.

2.3. Calculation of Ekman Pumping

To understand the impact of variability of sea ice distribution and atmospheric forcing such as wind on the mCDW circulation and thickness, Ekman pumping (EP) was calculated in the DGT for the period from January 2003 to December 2019 at 0.25° resolution. In polar seas, total ocean surface stress is a function of both wind and sea ice stresses, as sea ice drift and roughness can vary substantially from a simpler wind-ocean interface (Kim et al., 2017). Therefore, to calculate EP, we used the hourly 10-m wind field above the sea surface and daily mean sea ice motion obtained from the ERA5 data of the ECMWF reanalysis project (Hersbach et al., 2018) and Polar Pathfinder Daily 25 km EASE-Grid Sea Ice Motion Vectors Version 4 (Tschudi et al., 2019). Sea ice concentration data were obtained from three different sensors (AMSR-E, SSMIS, and AMSR-2) according to the period of interest (Spreen et al., 2008). The EP velocity, w_E, was calculated by the curl of the surface stress as follows:

$$w_E = \frac{1}{\rho_w f}\left(\frac{\partial \tau_o^y}{\partial x} - \frac{\partial \tau_o^x}{\partial y}\right) \tag{7}$$

where f is the Coriolis parameter, $\tau_o{}^x$ and $\tau_o{}^y$ represent the stress at the ocean surface, and ρ_w is the surface seawater density (1,026 kg m^{-3}). The ocean surface stress in each grid was calculated as a combination of sea ice and wind stress, considering the sea ice concentration (A), as follows:

$$\tau_o = A\tau_{io} + \left(1 - A\right)\tau_{ao} \tag{8}$$

where τ_{ao} and τ_{io} represent the ocean surface stress at the air–ocean and ice–ocean interfaces, respectively. In turn, these were calculated as follows:

$$\tau_{ao} = \left(\tau_{ao}^x, \tau_{ao}^y\right) = \rho_a C_{D,ao}\left|W_{10}\right|W_{10} \tag{9}$$

$$\tau_{io} = \left(\tau_{io}^x, \tau_{io}^y\right) = \rho_w C_{D,io}\left|U_{\text{ice}} - U_w\right|\left(U_{\text{ice}} - U_w\right) \tag{10}$$

where (τ^x, τ^y) are the zonal and meridional components of wind and ice–ocean stress, respectively; ρ_a is the density of air (1.29 kg m^{-3}); W_{10} is the wind velocity vector 10-m above the sea surface; U_{ice} is the sea ice velocity; and U_w is the current velocity at the sea surface. The observed surface current data is very limited. It is impossible to estimate the surface current from satellites because the study area is covered by sea ice in most seasons except summer. Therefore, in this study, the surface current was calculated assuming that a full Ekman spiral developed by the stresses is introduced into the ocean by wind and sea ice drift (Ekman, 1905; Kim et al., 2017; Pond & Pickard, 1983). However, this calculation may contain some errors in transferring the energy from the atmosphere and sea ice to the ocean because this calculation does not consider the various types of sea ice and uses wind reanalysis. The drag coefficient between the air and ocean ($C_{D,ao}$) was calculated depending on the wind speed (Large & Pond, 1981). The drag coefficient between sea ice and the ocean ($C_{D,io}$) is determined by the sea ice roughness (e.g., Häkkinen, 1986; Leppäranta & Omstedt, 1990; McPhee & Smith, 1976), concentration, length, and thickness (Lu et al., 2011). Therefore, this coefficient varies greatly according to regional characteristics. The horizontal distribution of the drag coefficient between the sea ice and ocean in the DGT was calculated from the ICESat sea ice thickness (Kurtz & Markus, 2012) and wind field. The calculated $C_{D,io}$ in DGT was distributed in the range of 0.004–0.01, and it was greater in front of DIS than at the DGT entrance.

2.4. Calculation of Buoyancy Flux

The air-sea heat and freshwater exchange at the sea surface play an important role in determining the upper ocean's stability, and modifying water properties. In particular, the production (wintertime brine rejection) and reduction (summertime melting) of sea ice lead to the variability of buoyancy flux at the sea surface around Antarctica (Sun, et al., 2016). Ocean surface warming by heat input and freshening by sea ice melting and input of the glacial meltwater creates a buoyant ocean surface layer and increase stratification. Conversely, surface cooling and sea ice production create a dense ocean surface layer and increase vertical convection. Webber et al. (2017) reported that the seasonal deepening of the warm mCDW layer in front of PIG was due to an increased local surface buoyancy flux and amplified upper ocean convection. Buoyancy flux (B_0) at the sea surface is the sum of heat (B_{HF}) and freshwater (B_{FW}) components, and can be expressed as follows:

$$B_0 = B_{\text{HF}} + B_{\text{FW}} \equiv -g\alpha \frac{Q_{\text{HF}}}{\rho_w C_p} + g\beta Q_{\text{FW}} S_0 \tag{11}$$

where g is the gravitational acceleration (9.8 m s^{-2}), S_0 is the ocean surface salinity (assumed to be 34 PSU), c_p is the specific heat of seawater (4,190 J kg^{-1} K^{-1}). Q_{HF} (positive for ocean heat gain) and Q_{FW} (negative for ocean freshwater gain) are the net air-sea heat flux (W m^{-2}) and freshwater flux (m s^{-1}), respectively. α and β are the thermal expansion coefficient ($-\rho^{-1}\,\partial\rho/\partial T$) and the saline contraction coefficient ($\rho^{-1}\,\partial\rho/\partial S$), respectively. To calculate the buoyancy flux at the sea surface (34 PSU, 0°C), α is set to 5.1×10^{-5} K^{-1} and β is set to 7.9×10^{-4} (Sverdrup et al., 1942).

Obtaining broad scale, high accuracy net ocean surface heat flux (Q_{HF}) and freshwater flux (Q_{FW}) around Antarctica is extremely difficult. In this study, we obtained them from the data-assimilating Southern Ocean State Estimate (SOSE) for 1/3° or 1/6° horizontal resolution from 2005 to 2019 (Mazloff, et al., 2010; Verdy & Mazloff, 2017). The air-sea heat and freshwater exchange estimated from SOSE may differ from reality due to the
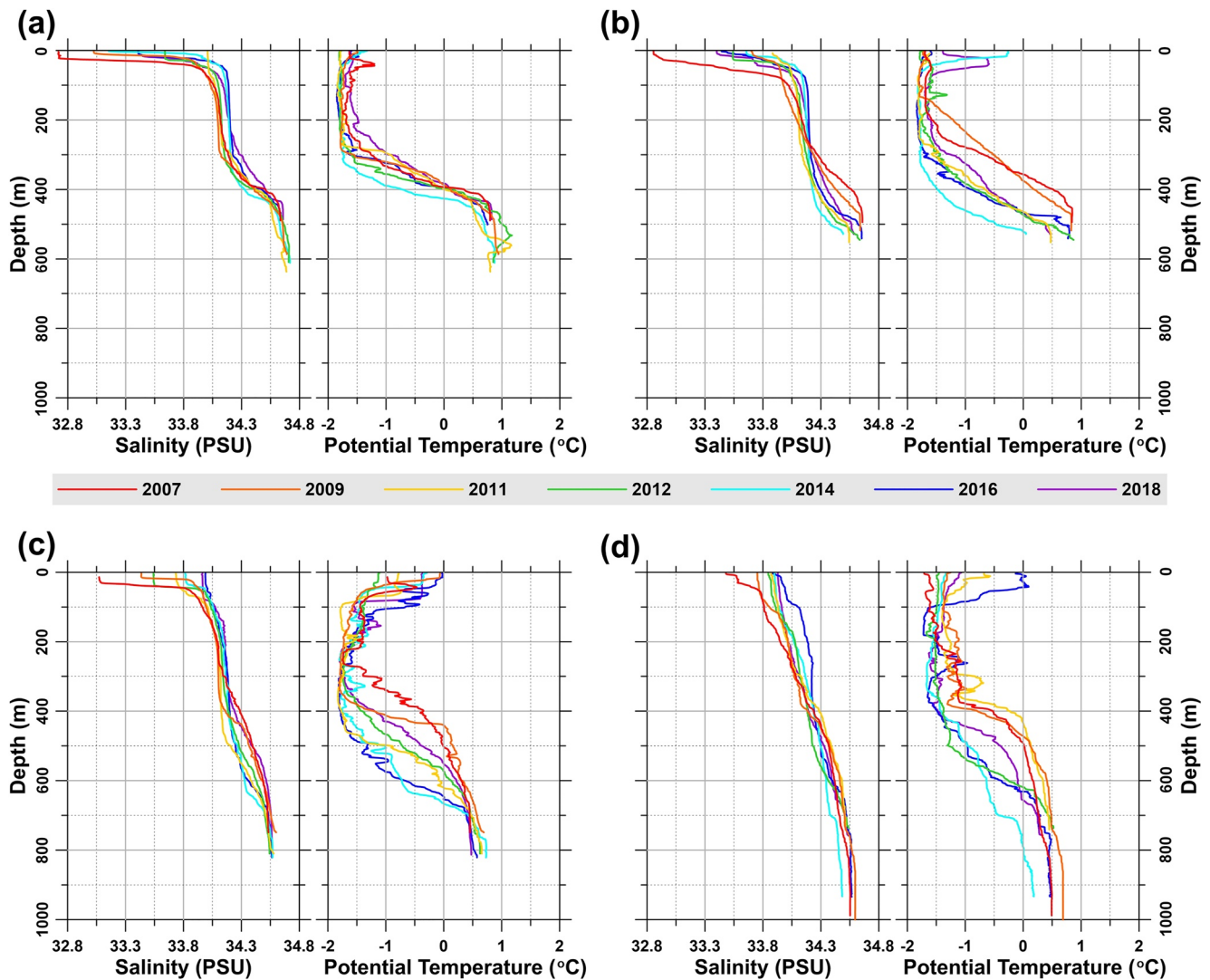
Figure 3. Vertical profiles of salinity and potential temperature during austral summer for seven nonconsecutive years at four sites (marked with magenta circles in Figure 1): (a) DGT entrance (magenta circles 1), (b) northern DGT (magenta circles 2), (c) Amundsen Sea polynya (magenta circles 3), (d) DIS front (magenta circles 4).

difficulty in constraining the sea ice fluxes and the variability of polynyas. Mazloff et al. (2010) estimated that in SOSE the seasonal variability of the estimated sea ice area in the Southern Ocean was slightly larger than observed, with a small phase difference, but the average difference was only 11%. Recent (after 2008) SOSE estimates have been further improved by assimilation of satellite-based sea ice concentration products (Verdy & Mazloff, 2017).

3. Results

3.1. Spatial and Interannual Variability of mCDW

The spatial and interannual variabilities of mCDW can be investigated from the observed temperature and salinity profiles in the DGT, in summer, between 2007 and 2018 (Figure 3). At the entrance of the DGT, mCDW generally occupied the depths below 400 m, while WW appeared at 50–300 m, overlaid by a fresh and warm AASW lens (Figure 3a). The thermocline depth separating mCDW and WW (300–400 m) shows little interannual variability, with fluctuation range <100 m, reaching a maximum in 2014, which is ∼50 m deeper compared to other years. Modified CDW temperature there oscillates between 0.75 and 1.2°C at the entrance of the DGT. On its way

southward along the DGT, mCDW is affected by external forcing (wind and sea ice) and mixing with other water masses (e.g., AASW and WW) driven by surface stress and buoyancy forcing. The interannual variability range of the thermocline depth between mCDW and WW increases consistently southward (Figures 3b and 3c). Just south of the shelf break, for example, the thermocline depth was actually shallower in 2007 and 2009 (Figure 3b) compared to the entrance of the DGT (Figure 3a), but it was deeper in other years, with again a maximum depth reached in 2014.

Further south, in the relatively deep and wide Amundsen Sea polynya (ASP), which formed in the summer to the north of the DIS (with a 1997–2010 average area of 27,300 ± 8,700 km^2 during the open period from October 1 to March 31; Arrigo et al., 2012), the thermocline depth variability, now reaching ∼250–300 m, is even more prominent (Figure 3c). Observations indicate that the AASW layer can experience a temperature change due to mixing with glacier and sea ice meltwater and heat exchange with the atmosphere, with a surface layer that is generally thicker in the polynya at the times of these summer surveys compared to their northern counterparts. Modified CDW in the polynya was also colder and fresher than at the DGT entrance; temperature and salinity oscillate between 0.4 and 0.7°C and between 34.5 and 34.6 PSU. In general, the thermocline depth tended to be >100 m deeper in the polynya (Figure 3c) than on the northern side of the trough (Figure 3b). This difference was particularly pronounced in 2016.

The last area visited by mCDW on its way to the DIS is the eastern slope of the DGT at the ice shelf front (Figure 3d). There, WW was warmer and fresher compared with the ASP in all years, likely influenced by glacial meltwater discharge diluted by the relatively warm mCDW. Moreover, the thermocline depth tends to be deeper due to strong downwelling caused by the influence of dominant easterly winds at the front of the DIS (Kim et al., 2016). In the summer of 2014, the temperature and salinity of mCDW significantly decreased in front of the DIS, reaching an observational low of 0.2°C. Excluding 2014, the interannual variability of the thermocline layer depth did not change significantly compared with the ASP (Figures 3c and 3d).

The shape of the thermocline and halocline separating the WW and mCDW layers were almost straight at the entrance of the DGT (Figure 3a), whereas they became concave up or down toward the south with a large and spatially consistent interannual variability component. In particular, in the ASP region, 2007, 2009, 2011, and 2018 showed concave down temperature profiles in the thermocline, while 2014 and 2016 profiles were concave up. The concave down temperature profile is consistent with the years when the thermocline depth between mCDW and WW was shallow. In contrast, the concave up temperature profile appears when the thermocline depth is deepened. Therefore, the concave down or up nature of the temperature profile is consistent with an upwelling of warm mCDW layer and a downwelling of cold WW layer, respectively. Both the phasing and the shape of the thermocline were maintained in front of the DIS.

The characteristics identified above in detailed regional and annual profiles are also apparent with broader spatial context in annual CTD sections along the DGT and the DIS front (Figure 4). In general, the isohalines and isotherms of the mCDW layer deepen southward along the DGT in all years, and interannual variability is large (Figures 4a–4g). In 2007, 2009, and 2011, the 34.3 PSU isohaline maintained a nearly constant 400 m depth from the entrance of the DGT to the front of the DIS. After 2012, the 34.3 PSU isohaline deepened southward, reaching 450–500 m depth close to the DIS, with signs of a potential rebound in 2018. In the deeper part of the water column, southward deepening of the isohalines (e.g., the 34.5 PSU isohaline) was a constant feature, but also with large interannual signals. For example, highly saline water (>34.5 PSU) was not found on the eastern slope in front of the DIS in 2014 (Figure 4e), pointing to a lack of supply of the denser water mass. In front of the ice shelf, the 34.3 PSU isohaline was located at a depth of ∼400 m in 2007, 2009, 2011, and 2018, but deepened in 2012, 2014, and 2016 (Figure 4h–4n). In the mean, the 34.5 PSU isohaline was relatively shallow on the eastern slope and deeper on the western slope, but also exhibited large interannual variability. In 2007, 2009, 2011, and 2012, dense, high salinity (>34.5 PSU) water was also observed above 800 m depth on the eastern slope, but its volume was substantially reduced in 2014, 2016, and 2018, with a minimum volume observed in 2014.

The interannual variability in the warm water volume in front of the DIS results in a change of heat transport into the ice shelf's cavity (Jenkins et al., 2018). In turn, the inflow of CDW into the DGT through other routes except for the entrance to DGT in the north is minimal. Therefore, the temperature and salinity of mCDW available to melt the ice are primarily determined by (a) north-south fluxes at the entrance of the DGT/continental shelf break where CDW floods the base and mixes with AASW and WW, and (b) local processes along mCDW southward
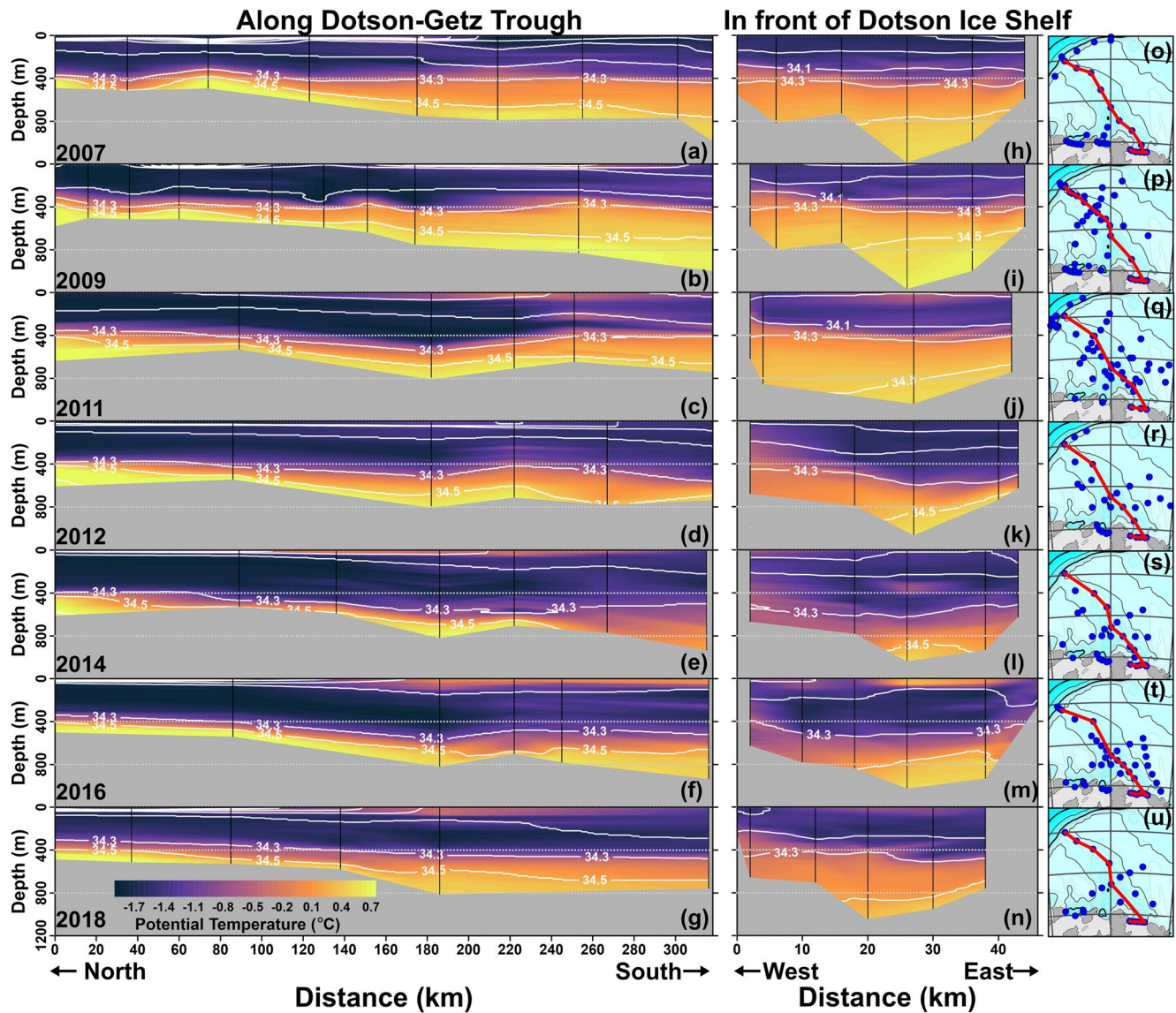
Figure 4. Distribution of potential temperature (graded color) and salinity (white lines) along the Dotson-Getz Trough (a, b, c, d, e, f, and g) and in front of the Dotson Ice Shelf (h, i, j, k, l, m, and n), as shown in red lines in the right panel.

path following the eastern flank of the trough (Ha et al., 2014) toward the DIS where the ratio of mCDW in the water column and its thickness can change via mixing with other water masses and convergence. As a first step to characterize heat content evolution, we quantify the mCDW volume along the DGT. The volume ratios of glacial meltwater, WW, and mCDW were calculated using Equations 4–6 and annually defined end members of each water mass (see Section 2.2).

Figure 5 shows the annual vertical profiles of the calculated volume ratios of mCDW, WW, and meltwater in four regions. By definition, the volume ratio of mCDW is minimal in the upper layer, and increased with depth to be close to 1 near the bottom. The vertical profile of the volume ratio of WW is opposite to that of mCDW, and the volume ratio of meltwater never exceeded 1.5%. Theoretically, the vertical volume ratios of mCDW, WW, and meltwater should be distributed between 0 and 1; however, in some cases, values deviated from this range due to calculation errors, either due to the influence of unconsidered water masses in Equation 3 (i.e., sea ice meltwater and AASW), or the assumption that the end members of the three water masses are constant for individual years (Table 2). If the residence time of mCDW in the DGT is longer than several months, the end member of mCDW could indeed show seasonal changes, increasing error in our volume ratio calculations. A third source of error is
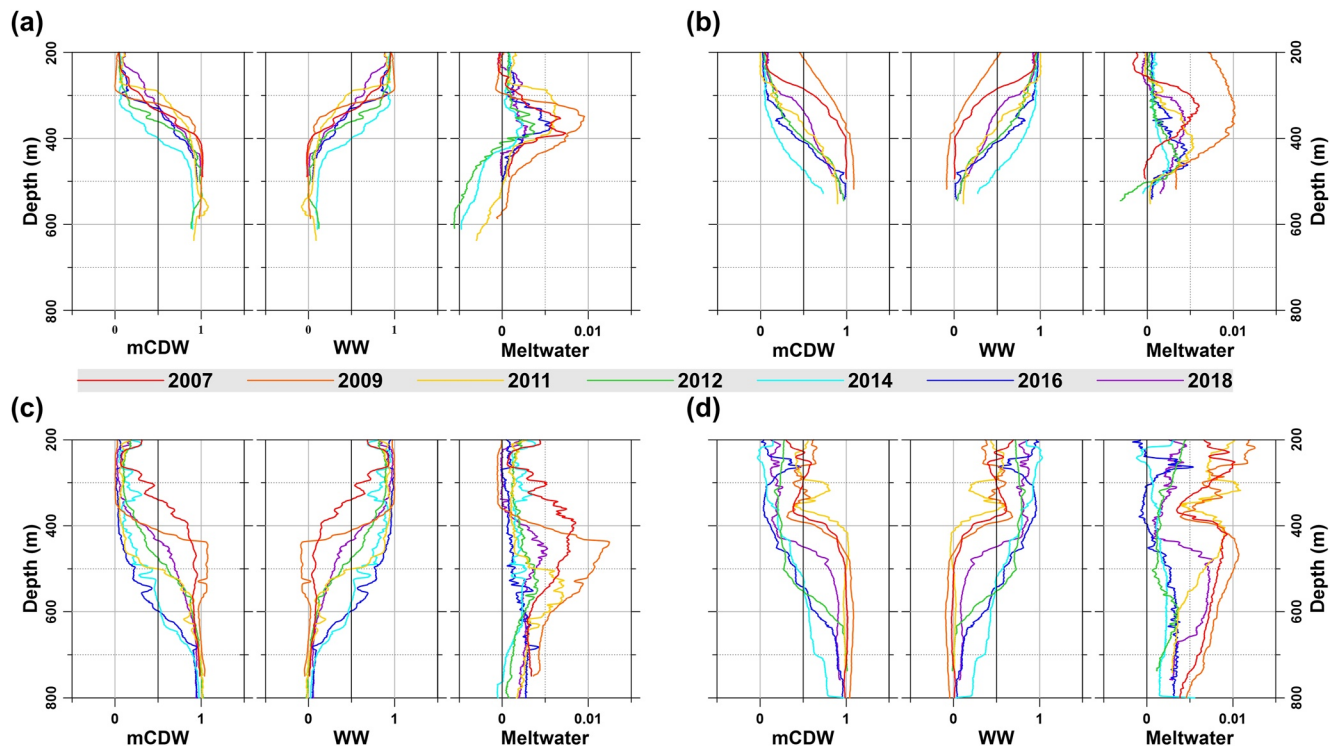
Figure 5. Vertical profiles of the estimated volume ratios of mCDW, winter water (WW), and glacial meltwater for seven nonconsecutive years at four sites: (a) the entrance of the Dotson-Getz Trough, (b) northern side of the Dotson-Getz Trough, (c) the center of the Amundsen Sea polynya, (d) and in front of the Dotson Ice Shelf (marked with magenta circles in Figure 1).

an implicit assumption that all mCDW in the DGT is sourced from the entrance of the DGT; however, mCDW in the Pine Island-Thwaites Trough with different characteristics (relatively higher temperature and salinity) could also be advected westward around Bear Ridge into the DGT.

Despite these caveats, volume ratios offer an interesting and somewhat novel perspective on interannual fluctuations in the DGT. As expected, variability in the vertical profile of the mCDW volume ratio at the entrance of the DGT was similar to that of the temperature profile in Figure 3. Although the volume ratio of meltwater is close to 0.01 at intermediate depth, it remains small compared with the volume ratios of mCDW and WW, so that we can define the mCDW volume ratio of 0.5 ("0.5mCDW"), the depth at which mCDW and WW have a similar ratio, as the upper boundary of mCDW layer. At the entrance of the DGT, the 0.5mCDW was located at a depth of 300–400 m (Figure 5a). It was shallowest in 2011 and deepest in 2014, with an interannual variability range of ~100 m. In the northern DGT region, the interannual variability range of the depth of the 0.5mCDW increased to ~260 m, reaching its shallowest point in 2009 (220 m), and its deepest in 2014 (480 m). The same isoline deepened further south in all years at the center of the ASP, 0.5mCDW deepened more than 100 m compared to the northern DGT in 2007, 2011, 2014, and deepened the most in 2016.

In front of the DIS, defining the depth of the 0.5mCDW layer was complicated by the presence of more significant meltwater intrusions at depths of 200–400 m in 2007, 2009, and 2011, associated with an increasing in the outflow of glacial meltwater and mixing with WW (Figure 5d). During periods with a thick mCDW layer, an increase in the available heat content in front of and under the ice shelf would have accelerated basal melting. Furthermore, the mCDW introduced into the ice shelf cavity is mixed with the glacial meltwater, decreasing density, and is discharged to the upper layer. The mCDW layer with high volume ratio (>0.75) occupies depths ranging from 400 m to the bottom in 2007, 2009, and 2011 in front of the DIS, and a significant volume of warm mCDW might have been supplied to the DIS, causing higher basal melting (Jenkins et al., 2018). However, after 2012, the 0.5mCDW layer deepened to below 500 m before rebounding again in 2018 to 450 m.

The southward increase of the interannual variability range in mCDW volume ratio is also shown in annual sections (Figures 6a–6g). In 2007, 2009, and 2011, the layer with a mCDW volume ratio >0.9 ("0.9mCDW") was
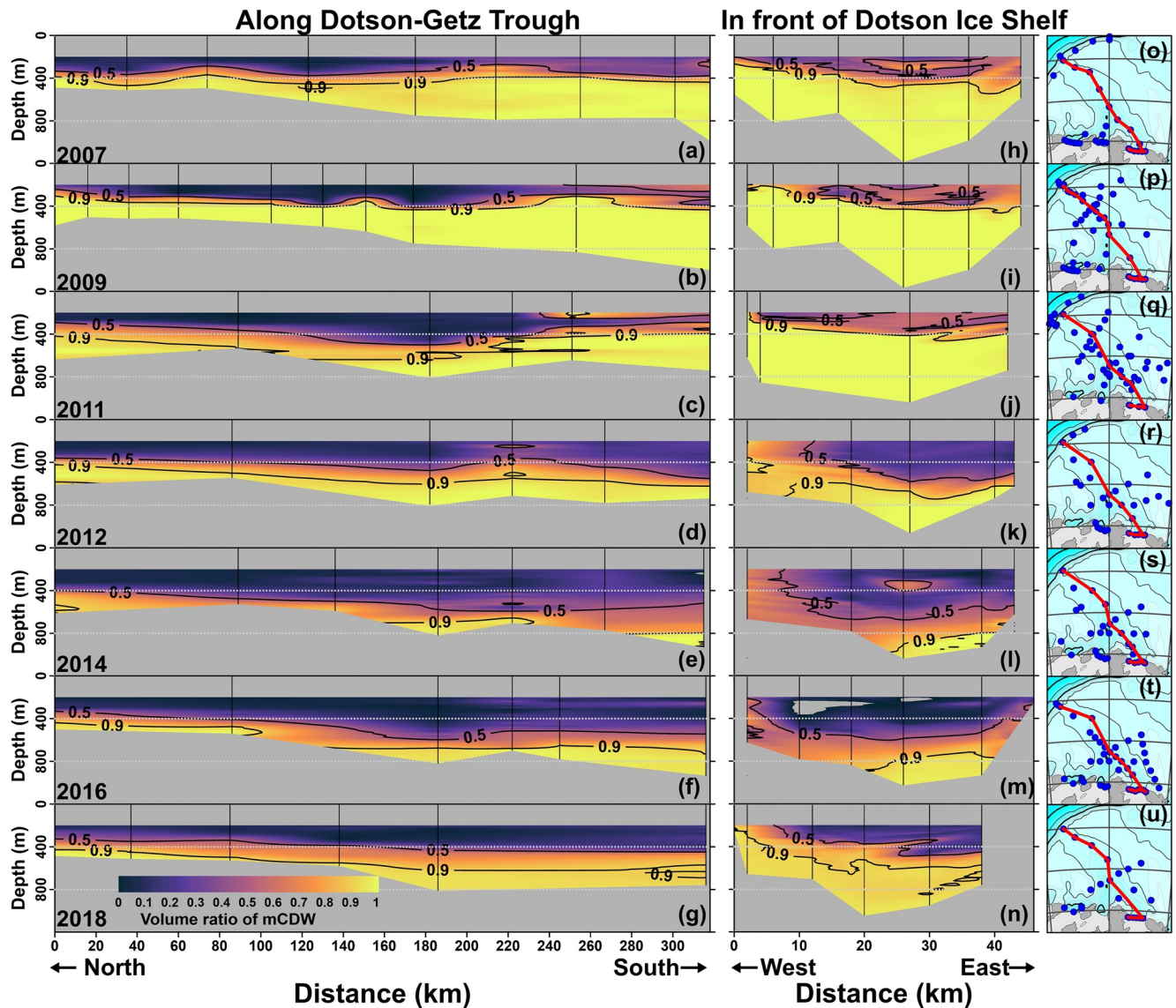
Figure 6. Distribution of the estimated volume ratio of mCDW along the Dotson-Getz Trough (a, b, c, d, e, f, and g) and in front of the Dotson Ice Shelf (h, i, j, k, l, m, and n), as shown in red lines in the right panel.

slightly deepened in the center of the ASP in comparison to most everywhere along the DGT, but it shallowed again in front of DIS (~400 m). However, after 2012, the 0.9mCDW layer thinned toward the south, with its top dipping below 600 m in front of the DIS. In 2014, a very thin 0.9mCDW layer was only observed below 800 m (Figures 6e and 6l). The same deep and warm layer thickness rebounded in 2018, indicating a distinct interannual variability of the mCDW volume in front of the ice shelf (Figures 6h–6n). In 2007, 2009, and 2011, a high volume ratio of mCDW (>0.9) was widely distributed from a depth of 400 m to the bottom. Its thickness decreased in 2012, reached a minimum in 2014, and progressively increased after 2016. In 2018, the 0.9mCDW region occupied a depth of 600 m to the bottom, similar to the distribution to that in 2012.

Below 500 m, the isohalines and isotherms generally shallow toward the eastern slope in front of the DIS, consistent with a geostrophic shear and the intrusion of mCDW into the DIS cavity along the eastern slope (Figures 4h–4n). The upper part of the water column is much more variable in terms of geostrophic shear, but a prominent feature is an increased mCDW volume ratio within the upper 400 m on the westernmost slope compared to the eastern slope associated with the outflow of a mixture of mCDW and glacial meltwater (Figures 6h–6n). As noted

earlier, the mCDW volume ratio was higher than 0.9 within the upper 400 m of the western slope in 2007, 2009, 2011, and 2018.

To quantify the interannual variability of the spatial distribution of the mCDW volume, we first calculated the absolute thickness of mCDW (AT_{mCDW}) from the vertical integration of the mCDW volume ratio (from 200 m to bottom) at each station for the studied years as follows:

$$AT_{mCDW} = \int_{200\,m}^{bottom} V_{mCDW} dz \qquad (12)$$

where V_{mCDW} is the volume ratio of mCDW calculated using Equation 6. The calculated AT_{mCDW} in the deep DGT center is larger than at the eastern slope, which is the main southward mCDW pathway toward DIS. Similarly, the AT_{mCDW} increased significantly in the deep DIS front compared to the shallow DGT entrance. These spatial variations result from the dependence on the volume ration on seabed depth. To more efficiently and quantitatively identify the spatio-temporal variability of mCDW, the absolute depth of the mCDW layer (AD_{mCDW}) was calculated from the difference between the bottom depth of CTD profiles of each station (d) and the AT_{mCDW} as follows:

$$AD_{mCDW} = d - AT_{mCDW} \qquad (13)$$

Figures 7a–7g shows the AD_{mCDW} at each station and its spatial distribution horizontally interpolated for each year, in which the DGT is defined as the region where the seabed was below a depth of 500 m. In 2007, the AD_{mCDW} varied between 250–490 m over the area of the DGT (Figure 7a). Relatively sparse spatial sampling between the entrance of the DGT and the center of the ASP prevents an analysis of zonal gradients in AD_{mCDW}. Further south (south of 73.5°S), the AD_{mCDW} was relatively shallow at the DIS front compared to the Getz Ice Shelf (GIS) front. The spatial distribution of the AD_{mCDW} values in 2009 was similar to that in 2007 (Figure 7b). In 2009, the spatial distribution of the AD_{mCDW} values interpolated horizontally from sufficient data across the DGT north of 73°S revealed the apparent difference between the eastern and western slopes of the trough. On the eastern slope of the DGT, which is the main pathway of mCDW, the AD_{mCDW} was 260 m (relatively shallow, top of mCDW layer), whereas it was ~395 m on the western slope (relatively deep, top of mCDW layer). To the north of the DIS, the AD_{mCDW} was shallower than 310 m, with the shallowest value of 204 m appearing at the westernmost point in front of the DIS.

In 2011, the AD_{mCDW} was deeper than that in 2007 and 2009 to the north of 73.5°S, while it was similar to that in 2009 just north of the DIS. Two observation points (to the left and right of Wright Island, Figure 1) in front of the GIS indicated that the AD_{mCDW} was deeper than 500 m at both stations. In particular, the deepest AD_{mCDW} (575 m) appeared to the west of Wright Island. In 2012, the AD_{mCDW} at the center of the ASP was slightly shallower than that in 2011, but it was 150 m deeper than that in front of the DIS in 2011. The shallowest AD_{mCDW} (260 m) was observed in the westernmost part of the DIS. In 2014 and 2016, the AD_{mCDW} was considerably deeper than previously across the entire DGT. In 2014, the AD_{mCDW} varied between 374–622 m over the area of the DGT, and shallowed slightly to 316–605 m in 2016. In particular, the AD_{mCDW} deepened remarkably at the center of the ASP and in front of the DIS compared with before 2014. Finally, the AD_{mCDW} shallowed again in 2018, presenting a horizontal distribution range of 279–527 m in the DGT. In addition, the AD_{mCDW} clearly shallowed at the westernmost part of the DIS and around the Martin Peninsula.

Figure 7h shows the horizontal distribution of the temporal mean and standard deviation of the interpolated AD_{mCDW} (Figures 7a–7g) at each grid point in the DGT. The mean AD_{mCDW} was <375 m at the entrance of the DGT and in front of the DIS, whereas it was >400 m at the center of the ASP and in front of the GIS. Notably, the mean AD_{mCDW} was relatively shallow on the eastern slope of the DGT, with a difference of 50 m in comparison to the western slope. The standard deviation of the AD_{mCDW} was the lowest (<50 m) at the entrance of the DGT and increased southwards. In front of the DIS, the standard deviation of the AD_{mCDW} was >100 m, and the maximum (>120 m) appeared in the westernmost point in front of the DIS due to the interannual variation in meltwater discharge. The irregular horizontal distribution of the standard deviation of the AD_{mCDW} suggests a spatial variation in the interannual variability of the mCDW volume.

Figures 8a and 8b presents the variation of the AD_{mCDW} along the DGT in each year and the interannual variation of the mean AD_{mCDW} in the DGT. The interannual variation range of the AD_{mCDW} at the entrance of the DGT was ~158 m (245–403 m), increasing to 230 m (347–577 m) at the center of the ASP, and then to 278 m (288–566 m)
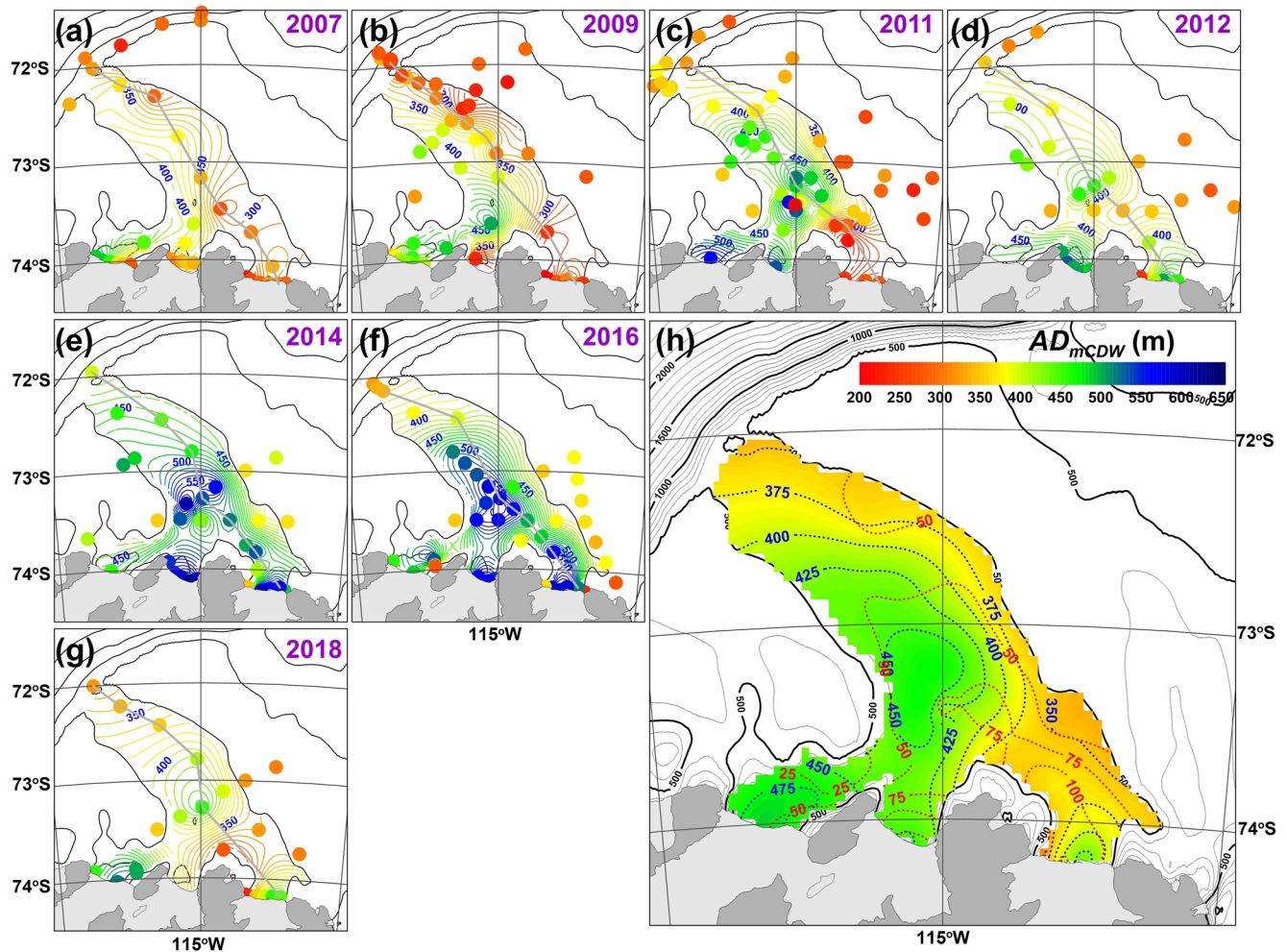
Figure 7. Spatial distribution of the calculated absolute depth of the mCDW layer (AD$_{mCDW}$) for seven nonconsecutive years (a–g). Color-coded symbols represent AD$_{mCDW}$ at CTD observation stations for each year. Color-coded contours represent the horizontal interpolated AD$_{mCDW}$ for each year. (h) Horizontal distribution of the temporal mean (blue dotted line) and standard deviation (red dotted line) of the interpolated AD$_{mCDW}$ at each grid point in the Dotson-Getz Trough (DGT).

in front of the DIS. This southward increase was due to a sharp decline in the mCDW volume in 2014 and 2016 at the center of the ASP and in front of the DIS, in contrast to 2007 and 2009. The spatial mean AD$_{mCDW}$ over the DGT was shallowest (354 m) in 2007 and deepest (479 m) in 2014 (Figure 8b). To estimate the volume of mCDW over the study area, the DGT was defined as the area where seabed depth is >500 m. The surface area thus defined is 25.6×10^3 km^2 (mean seabed depth: 664.5 m). From the mean AD$_{mCDW}$, seabed depth, and surface area, annual mCDW volume can be estimated. We find that the mCDW volume in the DGT in 2007 was ∼8,000 km^3, decreased rapidly in 2014 to ∼4,700 km^3, and increased to 7,300 km^3 in 2018.

3.2. Spatial and Temporal Variability of Ekman Pumping

Gradients in ocean surface stress from the atmosphere and sea ice can generate a local ocean circulation in the upper layer. In oceans without sea ice, the upwelling and downwelling processes can be influenced by the curl of the wind stress, the effect of which intensifies near the coast. However, in the polar region covered by sea ice, the wind stress is transferred to the ocean through sea ice, which can lead to substantial differences in parts where sea ice is not in free drift. Spatial imbalance of stress transfer can also be magnified at the sea ice margins due to the difference in the drag coefficient between the sea ice–ocean and air–ocean interfaces. Therefore, even homogeneous wind fields along the boundary of a polynya can generate spatial differences in ocean surface stress, creating local upwelling and downwelling. In the southern part of the DGT, the ASP develop in summer as strong winds
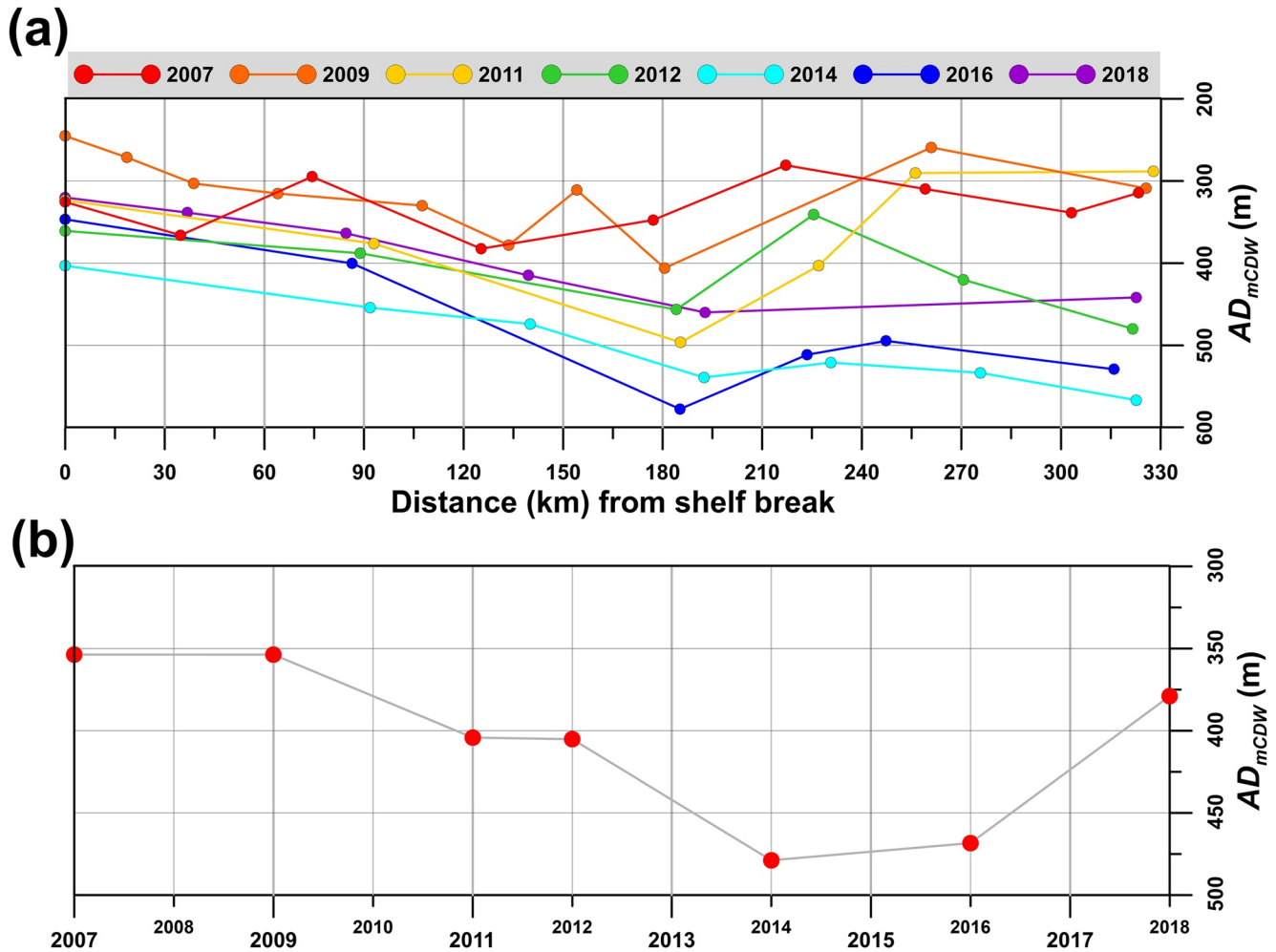
Figure 8. (a) Spatial variation of the AD_{mCDW} along the DGT in each year as shown in gray solid lines in the Figures 7a–7g. (b) Interannual variation of the spatial averaged AD_{mCDW} over the DGT.

and melt push the sea ice edge away from coast. The ASP is generally classified as wind-driven latent heat polynyas, but the upwelling of relatively warm meltwater mixed with mCDW to the surface also provides a sensible heat component (Stammerjohn et al., 2015). At the eastern boundary of the ASP, which is covered by heavy sea ice all year due to the grounded iceberg on the ridge (Mazur et al., 2019), a strong upwelling can be generated and the mCDW volume can increase. In the following, to understand the spatial imbalance of stress into the ocean and its influence on ocean circulation, EP was calculated using Equation 7 considering wind, sea ice motion, and sea ice concentration and thickness.

Figures 9a–9d shows the spatial distribution of seasonal EP in the DGT calculated from the daily mean EP for 17 years (2003–2019) including the sea ice concentration and wind. Southeasterly wind is dominant year-round in the DGT. The mean wind speed over 17 years was about 5 m s^{-1} in all seasons in front of the DIS, but decreases further north, reaching weak amplitudes at the entrance of the DGT. On the other hand, sea ice concentration exhibits significant temporal and spatial variations in the DGT. Climatologically, at the north of the DIS, an extensive polynya measuring ~240 km (east–west) by ~160 km (north–south) (based on the mean 0.2 sea ice concentration line over 17 years) forms in summer (December-January-February; Figure 9a). In autumn (March-April-May), the polynya contracts in the southeast direction (Figure 9b). Only a narrow area of open ocean/small sea ice concentration remains north of the BP in winter (June-July-August; Figure 9c), and the polynya expands again in the northwest direction in spring (October-September-November; Figure 9d).
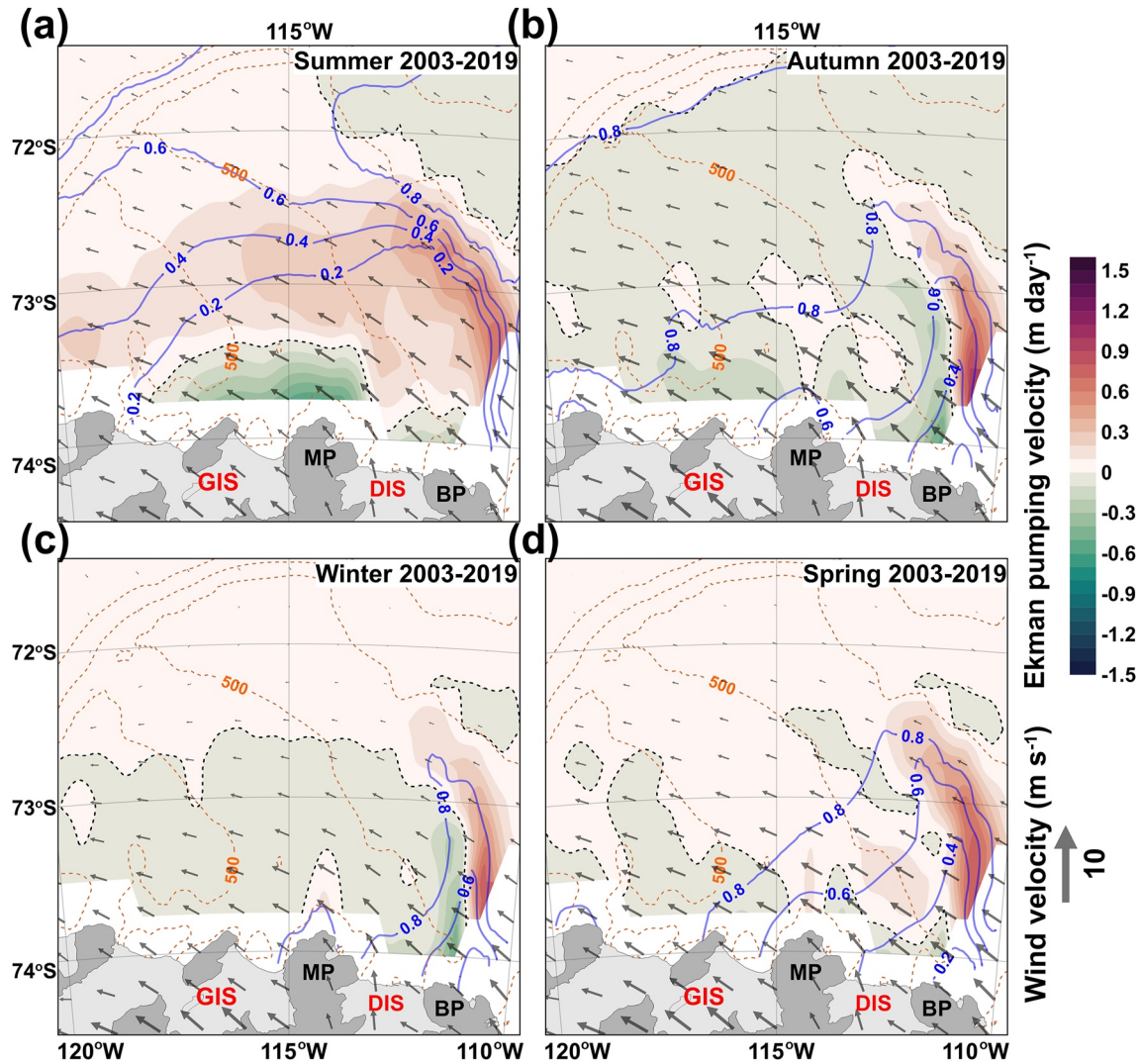
Figure 9. (a–d) Spatial distribution of seasonal Ekman pumping (EP) in the Dotson-Getz Trough (DGT) calculated from the daily mean EP over 17 years (2003–2019) including the sea ice concentration (blue solid contours) and wind (gray arrow). Black dash lines represent the zero EP.

Under the southeasterly wind field, upwelling is expected at the eastern and northern boundaries of the polynya owing to the steep gradient of the sea ice concentration. In contrast, downwelling occurs at the southern boundary. During the summer, strong upwelling (>0.5 m d^{-1}) appears at the eastern boundary, while strong downwelling dominates in front of the ice shelf (Figure 9a). However, relatively weak upwelling occurs in the northern ASP due to a decrease in easterly wind and an increase in sea ice concentration to the north. Near-zero values of EP are calculated during the other seasons with a weakly mobile sea ice cover (Figures 9b–9d). Strong upwelling occurred in all seasons along the eastern boundary of the polynya (111°W), where the sea ice concentration is nearly constant and immobile. In front of the DIS and to the north of the BP, the downwelling area exhibited a seasonal variability associated with the contraction/expansion of the polynya.

To better quantify the spatio-temporal variations of EP, we divided the DGT into 8 boxes, as shown in Figure 10a. At the entrance of the DGT (boxes A and B), the fluctuation range of EP was <± 0.15 m d^{-1}, except in the austral autumn of 2017, and the averaged daily EP was positive in all seasons except autumn (Figure 10b first panel). In autumn, the sea ice zone expands to the north, and the northern boundary of the sea ice zone tends to be located at the entrance of the DGT (Figure 9b), generating a weak downwelling. In general, a weak upwelling is observed in other seasons associated with homogenous sea ice cover and northerly decreasing easterly wind. The average
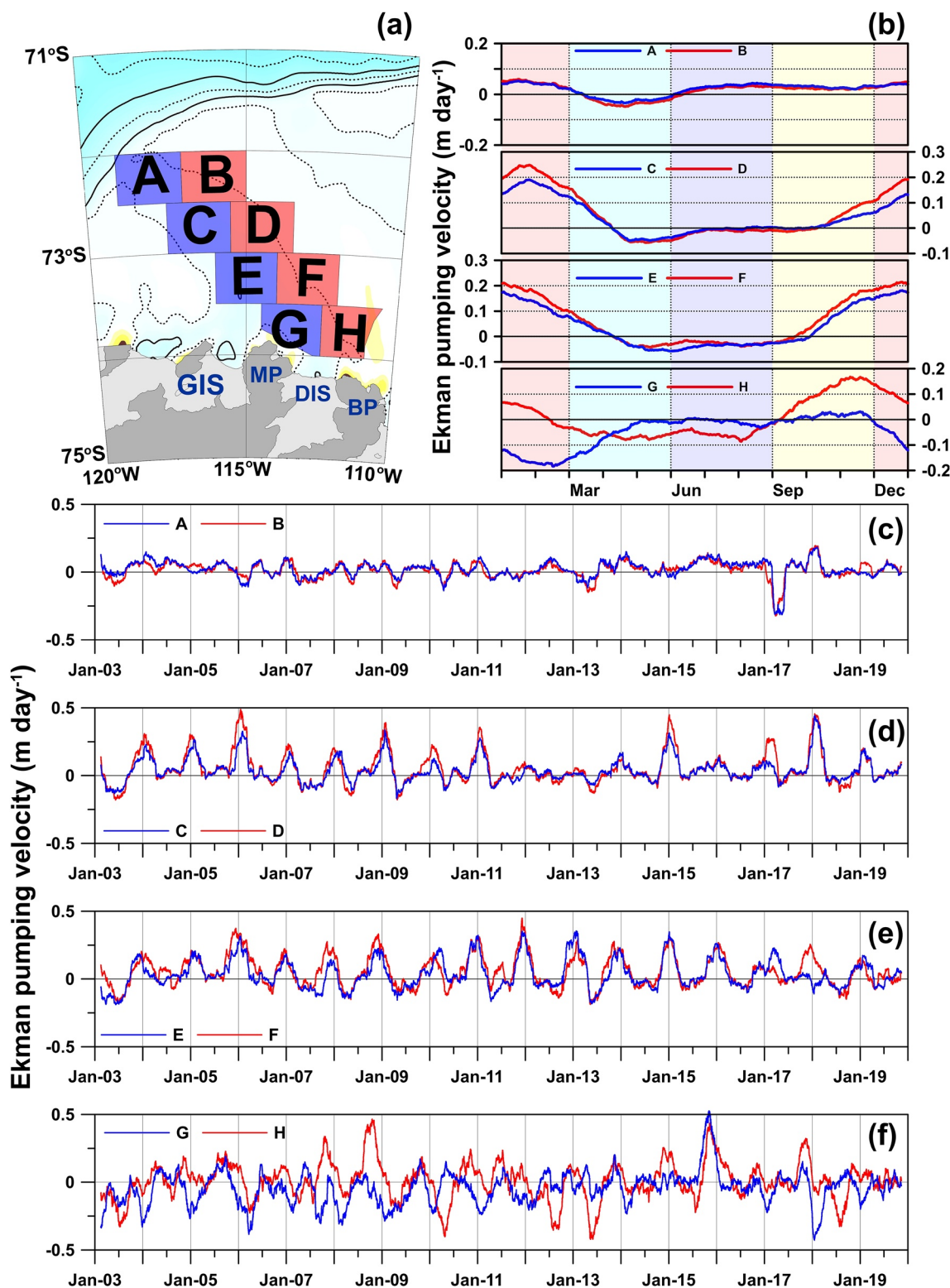
Figure 10. (a) The 8 boxes dividing the DGT, with those in blue (A, C, E, G) indicating the western slopes, and those in red (B, D, F, H) indicating the eastern slopes, respectively. (b) Climatological daily variation in EP averaged over 17 years in each box. (c–f) Timeseries variation of the 3 months running averaged EP in each box.

summer EP for 17 years is ~4 cm d^{-1} (Figure 10b first panel), indicating that the effect of the EP on the variability of the mCDW layer is insignificant at the DGT entrance.

The amplitude of the seasonal variability of EP increases further south along the DGT. Climatologically, EP in boxes C and D (the northern boundary of the ASP) presents a greater fluctuation compared to the entrance of the DGT, indicating distinct upwelling in spring and summer and weak downwelling in autumn and winter (Figures 10b and 10d). In the mean, the seasonal variation in EP there peaks at the end of January (Figure 10b second panel), with box D (0.25 m d^{-1}) being 0.06 m d^{-1} higher than box C (0.19 m d^{-1}). Further south, the variability of EP in boxes E and F located in the center of polynya shows similar seasonality to boxes C and D (Figure 10b). However, the maximum EP appears about a month earlier compared to boxes C and D, and the positive EP also occurs about a month earlier in spring (Figure 10b third panel). These fluctuations appear connected to the northward expansion of the polynya. Note that the EP in boxes C and D in the summer of 2012 and 2013 were less than 0.1 when the polynya did not expand as far north as usual (Figures A1i and A1j). During these two summers, EP in boxes E and F were higher than 0.2, similar to their overall summer mean (Figure 10e). Despite a zonal gradient along the trough (for example, there are greater fluctuations of EP in box F located on the eastern slope than box E of the western slope of the DGT in spring and summer), a strong zonal coherency is notable, demonstrated by a high correlation (coefficient of determination >0.63) in a linear regression between the daily EP at zonally adjacent boxes (A-B, C-D, and E-F). In particular, the coefficient of determination between boxes C and D was 0.78, the highest of all the correlations between the boxes.

The southernmost area (boxes G and H) is the one showing the most distinct zonal gradient and the most pronounced, though weak, phase difference from East to West (Figure 10b, lower panel). Positive EP occurred in box H (north of the BP) in spring and summer, but weak negative EP appeared in autumn and winter (Figure 10f). In particular, strong upwelling events >0.3 m d^{-1} dominated in November of 2007, 2008, 2015, and 2017. These upwelling events show up earliest in the south along the eastern slope of the DGT, then propagate northward, seemingly associated with the expansion of the polynya. In box H, EP increases in spring, peaks in November, and then gradually decreases (Figure 10b). In contrast, negative EP throughout the year except in spring was evident in box G, just northeast of the MP, where strong downwelling occurs under southeasterly wind and open water (no or very mobile sea ice) in summer. The statistically significant high correlation between zonally adjacent boxes in the north does not appear in between these southernmost boxes.

4. Discussion

The spatial variability of EP (Figure 10) is particularly apparent in summer when the polynya was widely developed. However, between 2003 and 2019, the annual maximum EP in summer of each year was not constant. For example, summer EP in box D increased steadily after 2004, reaching a maximum of 0.49 m d^{-1} in 2006, sharply declined in 2007 increased again in 2009 (0.4 m d^{-1}), and reached minima (0.15 m d^{-1}) in 2012, 2013, 2014 and 2016. Interannual variability of the seasonal cycle of EP in front of the ice shelf was much more complicated than that of the northern boxes. In box H, EP increased over the years until October 2008, with a maximum of 0.46 m d^{-1}, then weakened until 2015 and rebounded afterward. In comparison to its southern and northern vicinities, the summer EP at the center of the polynya showed relatively small interannual fluctuations. For example, in the summer of 2012, 2013, and 2014, there were no EP peak in boxes E and F, and G and H, but an upwelling of >0.3 m d^{-1} was observed in boxes E and F. We surmise the consistency of low summer sea ice concentration and associated lack of a sea-ice margin influence on the curl explain this difference.

An important result from our analyses is that an extensive decrease in summer upwelling at the southern and northern borders of the polynya in the DGT was observed in 2013 and 2014. To further analyze the effect of Ekman upwelling on the interannual variability of the mCDW volume in the DGT, timeseries of EP, surface fluxes and sea ice concentration along the eastern slope of the DGT are shown in Figure 11. In this area, the maximum and minimum EP occurred in summer and winter of each year, respectively, consistent with the seasonal variations discussed above (Figure 10b).

Air-sea heat and freshwater exchange at the sea surface can also affect the seawater density and vertical mixing. During summer, sea surface warming by heat input from the atmosphere and freshwater release by sea ice and icebergs melting reduce the density of the surface layer and stabilize the water column, hindering vertical convection. Conversely, cooling of the sea surface and brine rejection associated with sea ice formation during winter
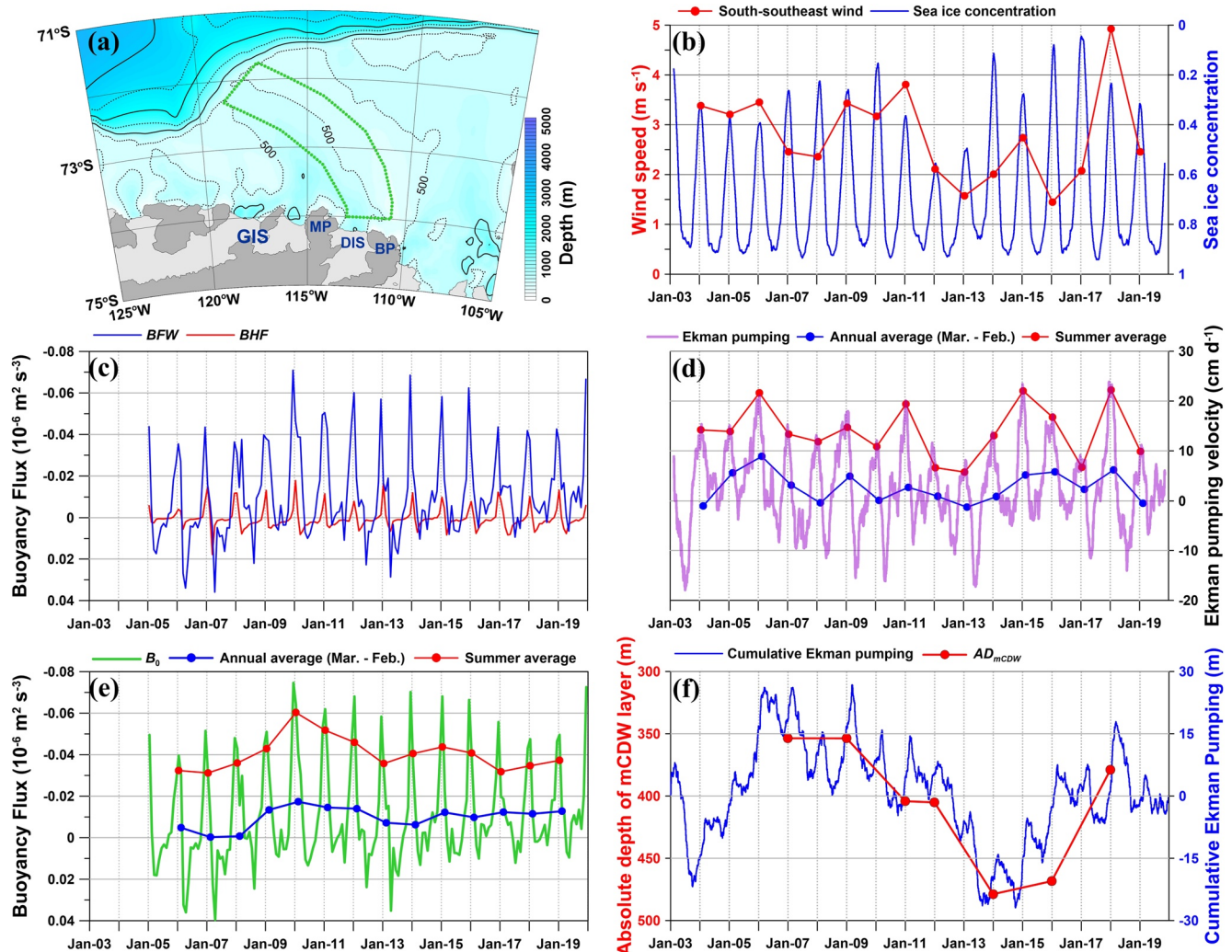
Figure 11. (a) A map indicating the area bounded by the green polygon for averaging wind speed, sea ice concentration, buoyancy flux, and Ekman pumping velocity in (b–f). (b) 3-month running mean of the sea ice concentration (blue line) and interannual variation of summer wind speed (red line). (c) Monthly average of surface heat flux (red line) and surface freshwater flux (blue line). (d) 3-month running mean/March to February average/Summer average of EP velocity (purple line/blue line/red line). (e) Monthly average (green line), March to February average (blue line), and summer average (red line) of total buoyancy fluxes. (f) Interannual variation of the absolute depth of the mCDW layer in the Dotson-Getz Trough (red line), and cumulative EP (blue line).

forms WW, weakens the stratification and invites vertical mixing; thereby thickening the WW layer and thinning the mCDW layer beneath it. Therefore, seasonal heat and freshwater flux at the sea surface can also cause the variability of thermocline depth between mCDW and WW (Webber et al., 2017). Here, we quantify the effect of surface heat and freshwater fluxes on the mCDW volume by calculating buoyancy fluxes of heat (B_{HF}) and freshwater (B_{FW}) in DGT using Equation 11 from 2005 to 2019 (Figure 11c), and comparing the sum of the fluxes to mCDW volume at interannual timescales (Figures 11e and 11f).

In DGT, the total surface buoyancy flux is mainly influenced by the seasonality of the freshwater flux due to the sea ice melt and production. In December or January of each year, a large amount of heat energy enters the ocean, accelerates sea ice melting and increases the freshwater content and buoyancy at the sea surface (i.e., decreases buoyancy flux from ocean to air). Inversely, sea ice formation associated with cooling in autumn and winter decreases buoyancy at the sea surface (i.e., increases buoyancy flux from ocean to air). The annually averaged buoyancy flux (from March to February) was lowest (-0.019×10^{-6} m² s⁻³) in 2010 (Figure 11e) following a minimum in summer buoyancy flux and the relatively high freshwater flux (2010 was anomalously low in sea ice concentration). The same quantity was closer to zero in 2007, 2008, 2013, and 2014 as relatively high buoyancy fluxes during winter and summer canceled each in the mean. Although the interannual variability of annual

average buoyancy flux does not seem sufficient to explain the higher volume of mCDW in 2007 and 2009, there is a similar trend to the mCDW volume, which decreased sharply from 2010 to 2014 and then increased again. Note, also, that EP depends on sea ice processes, as described above, such that sea ice impacts both the buoyancy flux and the stresses imparted at the ocean surface. Annual average buoyancy flux is mainly dependent on summer sea ice melting. In particular, in the summer of 2013, the polynya did not develop widely, perhaps because relatively weak winds did not push the sea ice away. As a result, an annual average EP was a minimum in DGT due to the gentle gradient of stress into the ocean at the sea ice margin by weak wind strength, and the absolute value of buoyancy flux was also relatively low due to the low sea ice melt rate.

To identify the effect of Ekman upwelling on the long-term variability of the mCDW volume, we removed its 17-year mean (2.8 cm d^{-1}) from the daily EP for the region defined as green polygon in Figure 11a and plotted the cumulative EP (Figure 11f). The cumulative EP increased continually from 2004, reaching its maximum in the summer of 2007. In 2008, it decreased slightly and increased again in 2009. After 2011, it continued to decrease reaching its minimum in 2015, rebounding again up until 2018. Although the amplitude of the long-term fluctuation of EP was relatively small (54 m) compared with that of the AD$_{mCDW}$ (125 m), their temporal correlation is remarkable, indicating a potential causation whereby change in mCDW volume is imparted by variation in EP in the DGT. Moreover, EP's annual averaged interannual variability largely depends on the summer EP (Figure 11d), the season with the greatest variability (Figure 10). Indeed, the interannual variability of summer averaged EP is determined by summer wind strength and the sea ice concentration in DGT (Figures 11b and 11d). Mean summer sea ice concentration from 2004 to 2019 was 0.29, with the maximum (0.56) and minimum (0.05) occurring in 2012 and 2017 (Figure 11b), respectively. Hence, sea ice concentration in the DGT showed a distinct interannual variability in summer, and the relatively high sea ice concentration (>0.5) and reduced polynya area in the summers of 2012 and 2013 would have weakened EP (Figure A1). On the other hand, summer sea ice concentration in 2014 and 2017 was climatologically low, and the ASP developed over a wide area; but, EP was not intense during those summers due to weak winds in the DGT. The south-southeast (SSE) wind, which parallels the eastern sea ice edge of the ASP, is dominant in the DGT and may therefore have an enormous impact on the variability of EP. In the summers of 2004, 2005, 2006, 2009, 2010, 2011, and 2018, the SSE wind was strengthened (>3 m s^{-1}) and caused an increase in EP in the DGT (Figures 11b and 11d). In contrast, the SSE wind was weakened (<2 m s^{-1}) in the summers of 2013, 2014, and 2016, thus decreasing EP. The minimum mean SSE wind speed in the DGT (1.5 m s^{-1}) occurred in the summer of 2016, while its maximum (4.9 m s^{-1}) was observed in 2018.

Although the maximum EP appeared in spring in the eastern slope of the DIS front, the seasonal variability of the spatially averaged EP in the DGT showed a maximum in summer. The strengthening of the SSE wind in summer along the sea ice margin generates ocean surface divergence and Ekman upwelling along the DGT; therefore can be lead to intrusion of mCDW at shelf break and causes an increase in the mCDW volume in DGT. In addition, the strength of the SSE wind in the DGT depends on the central location and pressure of the ASL. Affected by the SAM and ENSO phases, the ASL exhibits distinct seasonal east–west (Amundsen Sea–Ross Sea) shifts (Fogt et al., 2011; Hosking et al., 2013). The center of the ASL was located to the east of the DGT in the summers of 2004, 2009, 2010, 2011, and 2018, which strengthened the SSE wind, while it was located to the west of the DGT during the other years (Figure A2), which weakened the SSE wind. The longitudinal location of the center of the ASL in summer was significantly correlated ($r = 0.645$) with the strength of the SSE wind over 16 years (Figure 12b). Although the center of the ASL in 2004 and 2010 was located to the east of the DGT, the central pressure values were 985 and 982 hPa, respectively, which were weaker than 977 and 979 hPa in 2009 and 2011, respectively, and the SSE wind in the DGT was relatively weak (Figure 12a). In particular, the central pressure of the ASL in the summer of 2018 was 974 hPa, which was the strongest of the entire period and caused the strengthening of the SSE wind (>4.9 m s^{-1}) in the DGT. On the other hand, the center of the ASL was located to the west of 150°W in the summers of 2014 and 2017, when the central pressure values were 983 and 982 hPa, respectively, thus weakening the SSE wind. These results suggest that the interannual variability of the wind field, EP, and the mCDW volume can indeed be influenced by atmospheric circulation variability and the ASL.

5. Conclusions

Vertical temperature and salinity profiles were obtained from seven oceanographic surveys conducted along the Dotson-Getz Trough (DGT) between 2007 and 2018. A distinct interannual variability of the mCDW volume was observed along the DGT. The range of the interannual fluctuation in the thermocline depth separating mCDW
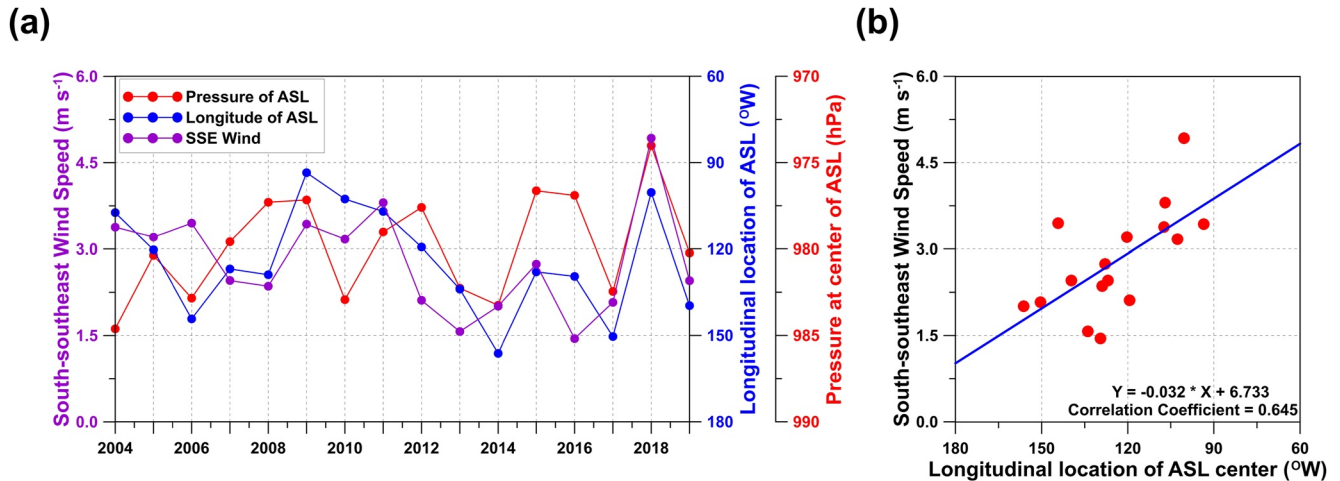
Figure 12. Interannual variation of the central pressure (red line) and longitudinal location (blue line) of the ASL with the strength of the south-southeast (SSE) wind (purple line) over the Dotson-Getz Trough (DGT) during summer (a); Correlation between the strength of the SSE wind over the DGT and longitudinal location of the ASL during summer (b).

and WW was less than 100 m at the entrance of the DGT, but increased to 250 m at the Amundsen Sea Polynya (ASP). The interannual variability of mCDW was quantitatively estimated by calculating the mCDW volume ratio and the absolute depth of the mCDW layer (AD_{mCDW}) in the DGT for each year. The spatial variation of the mean AD_{mCDW} (over the entire study period) did not change significantly along the eastern slope of the DGT from its entrance to the front of the Dotson Ice Shelf (DIS). However, the annual anomalies in AD_{mCDW} were significantly larger in front of the DIS (>100 m) compared to the entrance of the DGT (<50 m). The mean spatial AD_{mCDW} in the DGT deepened from 354 m in 2007 to 479 m in 2014, and then rebounded to 379 m in 2018. As a result, the mCDW volume in the DGT was about 8,000 km^3 in 2007, but decreased rapidly to ∼4,700 km^3 in 2014 before increasing again to ∼7,300 km^3 in 2018.

The mCDW that intrudes in the DGT at the shelf break appears to be affected by the local atmospheric circulation. In particular, steep gradients in the sea ice concentration at the boundary of the ASP in summer increase the spatial stress imbalance at the ocean surface, and cause strong Ekman pumping (EP). Interannual variation in both the wind strength over the polynya and the position of the sea ice-open ocean boundary in summer cause an interannual variability of EP in the DGT. In this study, to understand the effect of EP on the interannual variability of mCDW, we calculated EP in DGT by simplifying the process of energy transfer from the atmosphere and sea ice to the ocean. In this calculation, some variables (e.g., sea-ocean coefficient) were parameterized, and reanalyzed wind and estimated ocean current data were used due to limited observation data. However, despite many uncertainties in our EP calculation, the results appear to match the long-term variability of mCDW. The maximum cumulative EP in the DGT occurred in the summer of 2007, and subsequently decreased to a minimum in 2014 before increasing again in 2018. The difference in the cumulative EP between 2007 and 2014 was ∼54 m, which was smaller (but of similar order of magnitude) than the maximum interannual fluctuation of the AD_{mCDW} (125 m). Although the interannual variability of buoyancy flux in DGT is not sufficient to explain the long-term variability of mCDW, it shared a similar decreasing trend with the mCDW volume between 2010 and 2014.

In the DGT, the interannual variability of EP generally followed the south-southeast (SSE) wind variability. Strong upwelling was observed in the summers of 2006, 2009, 2011, and 2018, but weakened in 2012, 2013, and 2014. Meanwhile, the wind field in the DGT was related to the interannual variability in the position of the Amundsen Sea Low (ASL). In the summers of 2009, 2011, and 2018, strong upwelling occurred due to the strong SSE wind when the center of the ASL was located on the eastern side of the DGT with a relatively low central air pressure (<980 hPa). Inversely, in the summers of 2014 and 2017, upwelling was weakened due to the weak SSE wind in the DGT when the ASL was located in the Ross Sea with a high central air pressure (>980 hPa). We investigated the interannual variability of the mCDW in the DGT inflowing onto the continental shelf and its cause. We therefore identify an interesting new mechanism in which the interannual variability of mCDW in front of DIS previously revealed by Jenkins et al. (2018) could be explained by the variability of Ekman pumping de-

rived from local atmospheric circulation in DGT, seasonally modulated by the movements of the sea ice edge. This is complementary to theories that relate heat content variability to anomalous heat advection at the continental shelf break driven by changes in shelf break undercurrent amplitude and winds (Carvajal et al., 2013; Dotto et al., 2020; Kim et al., 2017; Thoma et al., 2008; Wåhlin et al., 2013). Since both shelf break winds and continental shelf winds share similar variability and drivers, further investigation is needed to detail the relative role of each in dictating the interannual variability of mCDW in front of DIS. Understanding the ocean's response to long-term atmospheric variability, such as climate change, based on theory complemented by this study, will lead to the identification of long-term trends in ice shelf melting and retreat due to oceanic heat transport into their cavity.
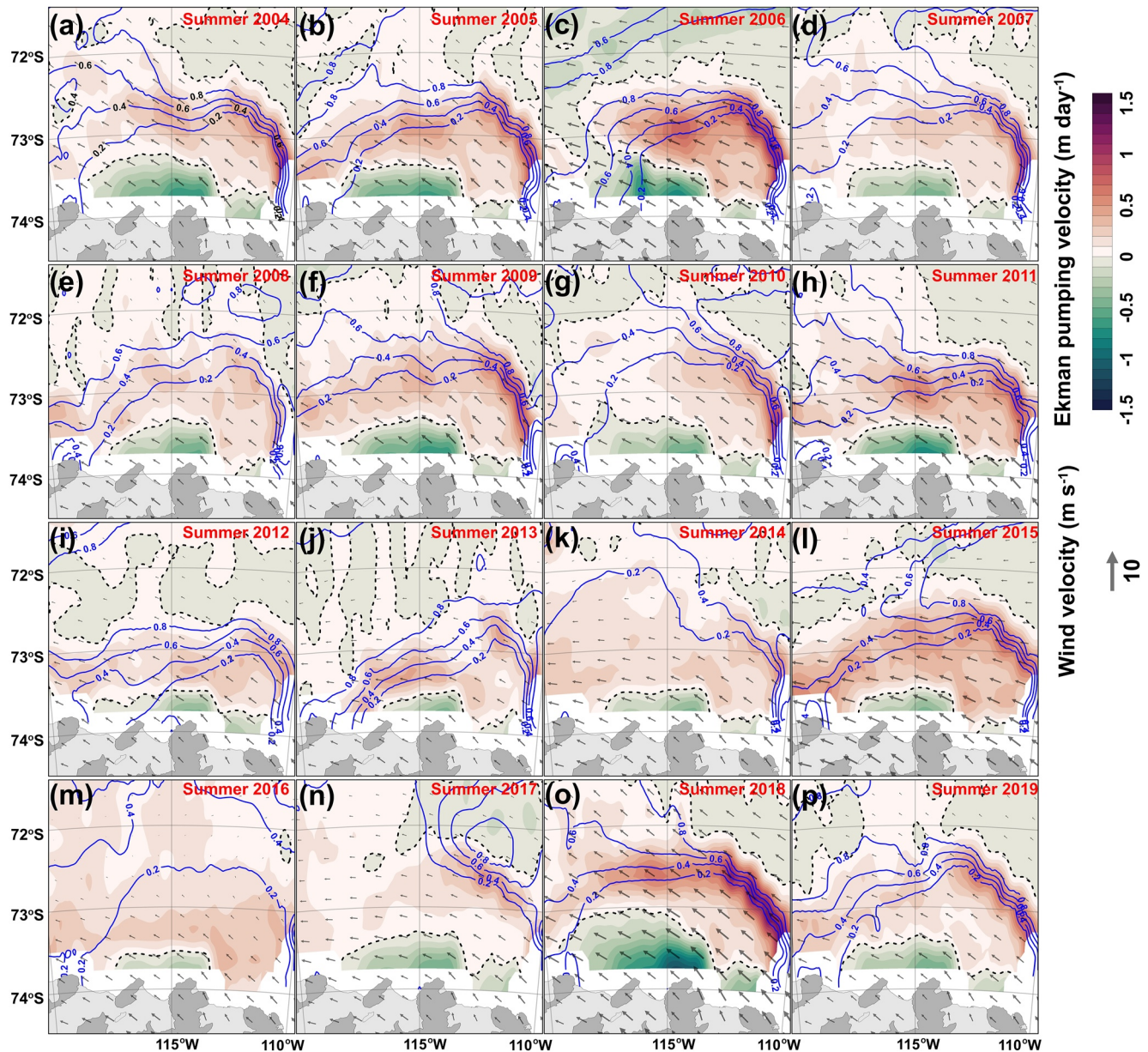
Appendix A

Figure A1. Spatial distribution of averaged EP, wind (gray arrow), and sea ice concentrations (blue solid contours) during summer from 2004 to 2019 (a–p). Black dash lines represent the zero EP.
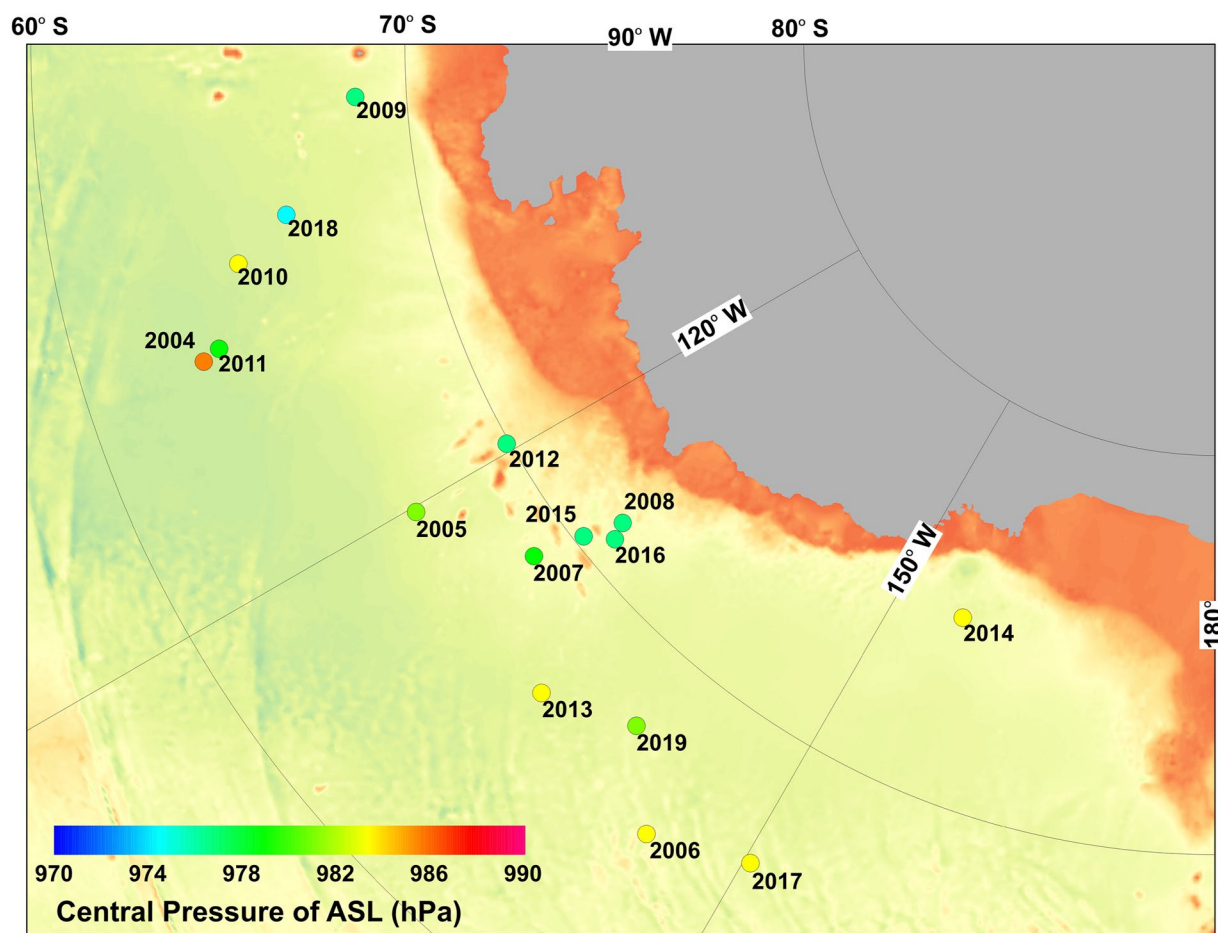
Figure A2. Location of the center of the Amundsen Sea Low (ASL) during summer and its central pressure.

Conflict of Interest

The authors declare no conflicts of interest relevant to this study.

Data Availability Statement

The seawater temperature, salinity, dissolved oxygen data are available from MGDS (Marine Geoscience Data System), SND (Swedish national Data Service), and KPDC (Korea Polar Data Center) according to the each cruise (NBP0702: https://www.marine-geo.org/tools/entry/NBP0702; NBP0901: https://www.marine-geo.org/tools/entry/NBP0901; NBP1005: https://www.marine-geo.org/tools/entry/NBP1005; Oden 2008/09: https://snd.gu.se/en/catalogue/study/ecds0203; Oden 2010/11: https://snd.gu.se/en/catalogue/study/ecds0204; ANA01C https://kpdc.kopri.re.kr/search/aba77f9f-5815-4a70-a411-59ebe35e7240; ANA02C https://kpdc.kopri.re.kr/search/50deac03-104e-4264-ad75-cafd4ca2f336; ANA04B https://kpdc.kopri.re.kr/search/2c489f38-6e59-4b38-b208-12359f0d3579; ANA06B https://kpdc.kopri.re.kr/search/c9b6fb99-04a0-48a8-b0ce-780f512c4f7f; ANA08B https://kpdc.kopri.re.kr/search/f511e827-d898-4cde-8d89-fe9a7b373e55). The wind data are available from CDS (Climate Data Store) website (https://cds.climate.copernicus.eu/cdsapp#!/dataset/reanalysis-era5-pressure-levels?tab=overview). The sea ice concentration data from AMSR-E, SSMIS, AMSR-2 are available from the Sea Ice Remote Sensing website of University of Bremen (https://seaice.uni-bremen.de/data/). Polar Pathfinder Daily 25 km EASE-Grid Sea Ice Motion Vector, Version 4 data are available from NSIDC (National Snow and Ice Data Center) website (https://nsidc.org/data/NSIDC-0116/versions/4). The reanalysis model data for net surface heat flux and freshwater flux are available from SOSE (Southern Ocean State Estimate) website (http://sose.ucsd.edu). Amundsen Sea Low indices data are available from website of Scott Hosking (https://scotthosking.com/asl_index#Data).

References

Adusumilli, S., Fricker, H. A., Medley, B., Padman, L., & Siegfried, M. R. (2020). Interannual variations in meltwater input to the Southern Ocean from Antarctic ice shelves. *Nature Geoscience*, *13*(9), 616–620. https://doi.org/10.1038/s41561-020-0616-z

Arrigo, K. R., Lowry, K. E., & van Dijken, G. L. (2012). Annual changes in sea ice and phytoplankton in polynyas of the Amundsen Sea, Antarctica. *Deep Sea Research Part II: Topical Studies in Oceanography*, *71*, 5–15. https://doi.org/10.1016/j.dsr2.2012.03.006

Biddle, L. C., Heywood, K. J., Kaiser, J., & Jenkins, A. (2017). Glacial meltwater identification in the Amundsen Sea. *Journal of Physical Oceanography*, *47*(4), 933–954. https://doi.org/10.1175/jpo-d-16-0221.1

Carvajal, G. K., Wåhlin, A. K., Eriksson, L. E., & Ulander, L. M. (2013). Correlation between synthetic aperture radar surface winds and deep water velocity in the Amundsen Sea, Antarctica. *Remote Sensing*, *5*(8), 4088–4106. https://doi.org/10.3390/rs5084088

Connolley, W. M. (1997). Variability in annual mean circulation in southern high latitudes. *Climate Dynamics*, *13*(10), 745–756. https://doi.org/10.1007/s003820050195

Depoorter, M. A., Bamber, J. L., Griggs, J. A., Lenaerts, J. T., Ligtenberg, S. R., van den Broeke, M. R., et al. (2013). Calving fluxes and basal melt rates of Antarctic ice shelves. *Nature*, *502*(7469), 89–92. https://doi.org/10.1038/nature12567

Dotto, T. S., Naveira Garabato, A. C., Bacon, S., Holland, P. R., Kimura, S., Firing, Y. L., et al. (2019). Wind-driven processes controlling oceanic heat delivery to the Amundsen Sea, Antarctica. *Journal of Physical Oceanography*, *49*(11), 2829–2849. https://doi.org/10.1175/JPO-D-19-0064.1

Dotto, T. S., Naveira Garabato, A. C., Wåhlin, A. K., Bacon, S., Holland, P. R., Kimura, S., et al. (2020). Control of the oceanic heat content of the Getz-Dotson Trough, Antarctica, by the Amundsen Sea Low. *Journal of Geophysical Research: Oceans*, *125*(8), e2020JC016113. https://doi.org/10.1029/2020JC016113

Dutrieux, P., De Rydt, J., Jenkins, A., Holland, P. R., Ha, H. K., Lee, S. H., et al. (2014). Strong sensitivity of Pine Island ice-shelf melting to climatic variability. *Science*, *343*(6167), 174–178. https://doi.org/10.1126/science.1244341

Ekman, V. W. (1905). *On the influence of the earth's rotation on ocean-currents*. Almqvist & Wiksells.

Fogt, R. L., Bromwich, D. H., & Hines, K. M. (2011). Understanding the SAM influence on the South Pacific ENSO teleconnection. *Climate Dynamics*, *36*(7–8), 1555–1576. https://doi.org/10.1007/s00382-010-0905-0

Gourmelen, N., Goldberg, D. N., Snow, K., Henley, S. F., Bingham, R. G., Kimura, S., et al. (2017). Channelized melting drives thinning under a rapidly melting Antarctic ice shelf. *Geophysical Research Letters*, *44*(19), 9796–9804. https://doi.org/10.1002/2017gl074929

Ha, H. K., Wåhlin, A. K., Kim, T. W., Lee, S. H., Lee, J. H., Lee, H. J., et al. (2014). Circulation and modification of warm deep water on the central Amundsen Shelf. *Journal of Physical Oceanography*, *44*(5), 1493–1501. https://doi.org/10.1175/JPO-D-13-0240.1

Häkkinen, S. (1986). Coupled ice-ocean dynamics in the marginal ice zones: Upwelling/downwelling and eddy generation. *Journal of Geophysical Research: Oceans*, *91*(C1), 819–832. https://doi.org/10.1029/JC091iC01p00819

Hersbach, H., Bell, B., Berrisford, P., Biavati, G., Horányi, A., Muñoz Sabater, J., et al. (2018). ERA5 hourly data on single levels from 1979 to present, Copernicus Climate Change Service (C3S) Climate Data Store (CDS). Retrieved from: https://cds.climate.copernicus.eu/cdsapp#!/dataset/reanalysis-era5-single-levels?tab=overview

Holland, P. R., Bracegirdle, T. J., Dutrieux, P., Jenkins, A., & Steig, E. J. (2019). West Antarctic ice loss influenced by internal climate variability and anthropogenic forcing. *Nature Geoscience*, *12*(9), 718–724. https://doi.org/10.1038/s41561-019-0420-9

Hosking, J. S., Orr, A., Marshall, G. J., Turner, J., & Phillips, T. (2013). The influence of the Amundsen–Bellingshausen Seas low on the climate of West Antarctica and its representation in coupled climate model simulations. *Journal of Climate*, *26*(17), 6633–6648. https://doi.org/10.1175/JCLI-D-12-00813.1

Jenkins, A. (1999). The impact of melting ice on ocean waters. *Journal of Physical Oceanography*, *29*(9), 2370–2381. https://doi.org/10.1175/1520-0485(1999)029<2370:tiomio>2.0.co;2

Jenkins, A., & Jacobs, S. (2008). Circulation and melting beneath George VI ice shelf, Antarctica. *Journal of Geophysical Research*, *113*(C4). https://doi.org/10.1029/2007jc004449

Jenkins, A., Shoosmith, D., Dutrieux, P., Jacobs, S., Kim, T. W., Lee, S. H., et al. (2018). West Antarctic ice sheet retreat in the Amundsen Sea driven by decadal oceanic variability. *Nature Geoscience*, *11*(10), 733–738. https://doi.org/10.1038/s41561-018-0207-4

Kim, C. S., Kim, T. W., Cho, K. H., Ha, H. K., Lee, S., Kim, H. C., & Lee, J. H. (2016). Variability of the Antarctic coastal current in the Amundsen Sea. *Estuarine, Coastal and Shelf Science*, *181*, 123–133. https://doi.org/10.1016/j.ecss.2016.08.004

Kim, T. W., Ha, H. K., Wåhlin, A. K., Lee, S., Kim, C. S., Lee, J. H., et al. (2017). Is Ekman pumping responsible for the seasonal variation of warm circumpolar deep water in the Amundsen Sea? *Continental Shelf Research*, *132*, 38–48. https://doi.org/10.1016/j.csr.2016.09.005

Kimura, S., Jenkins, A., Regan, H., Holland, P. R., Assmann, K. M., Whitt, D. B., et al. (2017). Oceanographic controls on the variability of ice-shelf basal melting and circulation of glacial meltwater in the Amundsen Sea Embayment, Antarctica. *Journal of Geophysical Research: Oceans*, *122*(12), 10131–10155. https://doi.org/10.1002/2017JC012926

Kurtz, N. T., & Markus, T. (2012). Satellite observations of Antarctic sea ice thickness and volume. *Journal of Geophysical Research*, *117*(C8). https://doi.org/10.1029/2012JC008141

Large, W. G., & Pond, S. (1981). Open ocean momentum flux measurements in moderate to strong winds. *Journal of Physical Oceanography*, *11*(3), 324–336. https://doi.org/10.1175/1520-0485(1981)011<0324:oomfmi>2.0.co;2

Leppäranta, M., & Omstedt, A. (1990). Dynamic coupling of sea ice and water for an ice field with free boundaries. *Tellus A: Dynamic Meteorology and Oceanography*, *42*(4), 482–495. https://doi.org/10.3402/tellusa.v42i4.11892

Lu, P., Li, Z., Cheng, B., & Leppäranta, M. (2011). A parameterization of the ice-ocean drag coefficient. *Journal of Geophysical Research*, *116*(C7). https://doi.org/10.1029/2010jc006878

Mazloff, M. R., Heimbach, P., & Wunsch, C. (2010). An eddy-permitting Southern Ocean state estimate. *Journal of Physical Oceanography*, *40*(5), 880–899. https://doi.org/10.1175/2009jpo4236.1

Mazur, A. K., Wahlin, A. K., & Kalén, O. (2019). The life cycle of small-to medium-sized icebergs in the Amundsen Sea Embayment. *Polar Research*, *38*. https://doi.org/10.33265/polar.v38.3313

McPhee, M. G., & Smith, J. D. (1976). Measurements of the turbulent boundary layer under pack ice. *Journal of Physical Oceanography*, *6*(5), 696–711. https://doi.org/10.1175/1520-0485(1976)006<0696:mottbl>2.0.co;2

Nitsche, F. O., Jacobs, S. S., Larter, R. D., & Gohl, K. (2007). Bathymetry of the Amundsen Sea continental shelf: Implications for geology, oceanography, and glaciology. *Geochemistry, Geophysics, Geosystems*, *8*(10). https://doi.org/10.1029/2007gc001694

Paolo, F. S., Fricker, H. A., & Padman, L. (2015). Volume loss from Antarctic ice shelves is accelerating. *Science*, *348*(6232), 327–331. https://doi.org/10.1126/science.aaa0940

Pond, S., & Pickard, G. L. (1983). *Introductory dynamical oceanography*. Gulf Professional Publishing.

Rignot, E., Mouginot, J., Morlighem, M., Seroussi, H., & Scheuchl, B. (2014). Widespread, rapid grounding line retreat of Pine Island, Thwaites, Smith, and Kohler glaciers, West Antarctica, from 1992 to 2011. *Geophysical Research Letters*, *41*(10), 3502–3509. https://doi.org/10.1002/2014GL060140

Shepherd, A., Ivins, E., Rignot, E., Smith, B., Van Den Broeke, M., Velicogna, I., et al. (2018). Mass balance of the Antarctic Ice Sheet from 1992 to 2017. *Nature*, *558*, 219–222.

Spreen, G., Kaleschke, L., & Heygster, G. (2008). Sea ice remote sensing using AMSR-E 89-GHz channels. *Journal of Geophysical Research: Oceans*, *113*(C2). https://doi.org/10.1029/2005JC003384

Stammerjohn, S. E., Maksym, T., Massom, R. A., Lowry, K. E., Arrigo, K. R., Yuan, X., et al. (2015). Seasonal sea ice changes in the Amundsen Sea, Antarctica, over the period of 1979–2014Seasonal sea ice changes in the Amundsen Sea. *Elementa: Science of the Anthropocene*, *3*. https://doi.org/10.12952/journal.elementa.000055

Sun, S., Eisenman, I., & Stewart, A. L. (2016). The influence of Southern Ocean surface buoyancy forcing on glacial-interglacial changes in the global deep ocean stratification. *Geophysical Research Letters*, *43*, 8124–8132. https://doi.org/10.1002/2016GL070058

Sverdrup, H. U. (1942). *The oceans, their physics, chemistry, and general biology*, In H. U. Sverdrup, M. W. Johnson, & R. H. Fleming (Eds.). Prentice-Hall.

Thoma, M., Jenkins, A., Holland, D., & Jacobs, S. (2008). Modelling Circumpolar Deep Water intrusions on the Amundsen Sea continental shelf, Antarctica. *Geophysical Research Letters*, *35*(18). https://doi.org/10.1029/2008GL034939

Tschudi, M., Meier, W., Stewart, J., Fowler, C., & Maslanik, J. (2019). *Polar Pathfinder daily 25 km EASE-Grid sea ice motion vectors, version 4, [2003-2019]*. NASA National Snow and Ice Data Center Distributed Active Archive Center. https://doi.org/10.5067/INAWUWO7QH7B

Turner, J., Orr, A., Gudmundsson, G. H., Jenkins, A., Bingham, R. G., Hillenbrand, C. D., et al. (2017). Atmosphere-ocean-ice interactions in the Amundsen Sea embayment, West Antarctica. *Reviews of Geophysics*, *55*(1), 235–276. https://doi.org/10.1002/2016RG000532

Verdy, A., & Mazloff, M. R. (2017). A data assimilating model for estimating Southern Ocean biogeochemistry. *Journal of Geophysical Research: Oceans*, *122*(9), 6968–6988. https://doi.org/10.1002/2016jc012650

Wåhlin, A. K., Kalén, O., Arneborg, L., Björk, G., Carvajal, G. K., Ha, H. K., et al. (2013). Variability of warm deep water inflow in a submarine trough on the Amundsen sea shelf. *Journal of Physical Oceanography*, *43*(10), 2054–2070. https://doi.org/10.1175/JPO-D-12-0157.1

Wåhlin, A. K., Muench, R. D., Arneborg, L., Björk, G., Ha, H. K., Lee, S. H., et al. (2012). Some implications of Ekman layer dynamics for cross-shelf exchange in the Amundsen Sea. *Journal of Physical Oceanography*, *42*(9), 1461–1474. https://doi.org/10.1175/JPO-D-11-041.1

Wåhlin, A. K., Yuan, X., Björk, G., & Nohr, C. (2010). Inflow of warm circumpolar deep water in the central Amundsen shelf. *Journal of Physical Oceanography*, *40*(6), 1427–1434. https://doi.org/10.1175/2010JPO4431.1

Webber, B. G., Heywood, K. J., Stevens, D. P., Dutrieux, P., Abrahamsen, E. P., Jenkins, A., et al. (2017). Mechanisms driving variability in the ocean forcing of Pine Island Glacier. *Nature Communications*, *8*(1), 1–8. https://doi.org/10.1038/ncomms14507